

Ambient Ion Trapping and Separations for High Throughput Structurally Selective Material Deposition

September 2020

Sandilya Garimella
Ailin Li
Venkateshkumar Prabhakaran
Adam Hollerbach
Yehia Ibrahim

DISCLAIMER

This report was prepared as an account of work sponsored by an agency of the United States Government. Neither the United States Government nor any agency thereof, nor Battelle Memorial Institute, nor any of their employees, makes **any warranty, express or implied, or assumes any legal liability or responsibility for the accuracy, completeness, or usefulness of any information, apparatus, product, or process disclosed, or represents that its use would not infringe privately owned rights.** Reference herein to any specific commercial product, process, or service by trade name, trademark, manufacturer, or otherwise does not necessarily constitute or imply its endorsement, recommendation, or favoring by the United States Government or any agency thereof, or Battelle Memorial Institute. The views and opinions of authors expressed herein do not necessarily state or reflect those of the United States Government or any agency thereof.

PACIFIC NORTHWEST NATIONAL LABORATORY
operated by
BATTELLE
for the
UNITED STATES DEPARTMENT OF ENERGY
under Contract DE-AC05-76RL01830

Printed in the United States of America

Available to DOE and DOE contractors from the
Office of Scientific and Technical Information,
P.O. Box 62, Oak Ridge, TN 37831-0062;
ph: (865) 576-8401
fax: (865) 576-5728
email: reports@adonis.osti.gov

Available to the public from the National Technical Information Service
5301 Shawnee Rd., Alexandria, VA 22312
ph: (800) 553-NTIS (6847)
email: orders@ntis.gov <<https://www.ntis.gov/about>>
Online ordering: <http://www.ntis.gov>

Ambient Ion Trapping and Separations for High Throughput Structurally Selective Material Deposition

September 2020

Sandilya Garimella
Ailin Li
Venkateshkumar Prabhakaran
Adam Hollerbach
Yehia Ibrahim

Prepared for
the U.S. Department of Energy
under Contract DE-AC05-76RL01830

Pacific Northwest National Laboratory
Richland, Washington 99354

Contents

1.	Introduction:	4
2.	Mass and Structure Selective Ion Soft-Landing:	5
2.1	High Ion Utilization Efficiency IMS/MS System Development	5
2.1.1	<i>Need for Concurrent Accumulation</i>	6
2.1.2	<i>Methods</i>	7
2.1.3	<i>Results and Discussion</i>	10
2.1.4	<i>Overall Utility</i>	18
2.2	Characterization of Structure and Mass Selected Molecules	21
3.	Ambient Ion Confinement	25
3.1	Experimental Details	26
3.1.1	<i>Simulation Parameters</i>	26
3.1.2	<i>Description of Rotating Waveforms</i>	26
3.1.3	<i>Electrospray and Mass Spectrometry</i>	27
3.1.4	<i>APIC Fabrication</i>	28
3.2	Results and Discussion	28
3.2.1	<i>Ion Trajectory Simulations</i>	28
3.2.2	<i>Theory of ion motion inside APIC</i>	32
3.2.3	<i>Experiments using helically rotating electric fields</i>	33
4.	Publications, Patents and Proposals	36

1. Introduction:

While ion mobility coupled to mass spectrometry (IMS/MS) has been increasingly adapted to biological analysis, the structural and molecular specificity offered by IMS/MS has untapped potential for creating novel materials (for energy, catalysis, biomolecular switches etc.) with rationally tailored properties by precisely controlling the chemical structure and composition of these materials. While electrochemical and catalytic properties of the bulk material are understood by mass-selective ion-soft-landing, different structures of one molecule can exhibit distinct properties from the bulk. Many biological phenomenon occur at interfaces and are highly structurally specific. IMS/MS offers means to separate molecules in a sample (which is first ionized and released to gas phase from the condensed phase) based on mass and structure. Species thus separated can potentially be deposited onto surfaces with molecular and structural specificity, to perform fundamental investigations for understanding critical interfacial phenomenon. Key performance metrics for IMS/MS analysis are resolution of separations and sensitivity. Recently developed Structures for Lossless Ion Manipulations (SLIM)⁴ enabled unprecedented resolution in IMS separations. In addition, high sensitivity was enabled in SLIM due to lossless confinement of ions using radio frequency fields. Thus, SLIM enabled extremely long path length separations (up to 0.1 km thus far) providing efficient separation of molecular ions never before achieved (e.g. isotopologues, D&L amino acids). While SLIM has unprecedented analytical separations power/utility, the use of SLIM platform for depositing mobility and mass selected molecular ions has two specific technological challenges: (a) Pulsed nature of IMS separations and their low duty cycle and (b) the need for a low vacuum of ~4 torr for lossless ion confinement. These limitations lead to long deposition times due to loss of ions generated from the sample. Enabling ion confinement at atmospheric pressure will be path-breaking contribution to the fundamental understanding of ion manipulations and separations and will also enable novel science currently precluded due to the inability of the present technologies to confine ions under ambient conditions. Traditionally used radio frequency fields are ineffective in confining ions at high pressures due to ion/neutral collisions. To address these, we propose to (a) develop methods for confining and manipulating ions for lossless IMS separations at atmospheric pressure enabling high sensitivity and throughput and (b) use the high specificity of IMS/MS and high throughput from ambient ion confinement to perform mobility and mass selective ion deposition at atmospheric pressure. Our goal is to enable the study of the fundamental properties of energy/catalysis materials and biomolecules. This project paves the way for high-throughput, mass and structure selective material deposition for highly specific surface creation/functionalization (discussed in Section 2 of the report). Further, the developments reported continue to push the boundaries of this process to ambient conditions (discussed in Section 3 of the report). We conclude with a list of specific intellectual property and publications which have been the outcome of this funded project.

2. Mass and Structure Selective Ion Soft-Landing:

The ability to separate ions based on their mass or structure has, in addition to analytical utility, application to synthesizing novel materials by depositing ions selectively onto surfaces. High performance IMS/MS separations and material collection at ambient conditions is a potentially promising direction. To efficiently be able to deposit molecules on a surface with structure and mass selectivity we report development of a high ion utilization efficiency method for performing IMS/MS analysis. This is a critical step in being able to deposit materials on a surface in useful quantities. IMS being a pulsed technique, traditionally uses only <5% of ions generated from continuous ions sources like electrospray ionization. We report a solution to this problem by our “concurrent ion accumulation and separation method” used with the Structures for Lossless Ion manipulations (SLIM) platform. This method was then used to deposit selected isomers of Poly-Oxo Metallates and study them using transmission electron microscopy (TEM), X-ray diffraction spectroscopy (XRD), Energy dispersive spectroscopy (ESD) and infra-red spectroscopy (IR). These two are discussed below in Section 2.1 and 2.2.

2.1 High Ion Utilization Efficiency IMS/MS System Development

Excerpt of title and abstract from a manuscript in final review:

“ION MOBILITY SPECTROMETRY WITH HIGH ION UTILIZATION EFFICIENCY USING TRAVELING WAVE-BASED STRUCTURES FOR LOSSLESS ION MANIPULATIONS (SLIM)

Authors: Ailin Li, Gabe Nagy, Christopher R. Conant, Randolph V. Norheim, Joon Yong Lee, Cameron Giberson, Adam L. Hollerbach, Venkateshkumar Prabhakaran, Issac K. Attah, Christopher D. Chouinard, Aneesh Prabhakaran, Richard D. Smith, Yehia M. Ibrahim, Sandilya V.B. Garimella*

*Corresponding Author: sandilya.garimella@pnnl.gov

In review: ACS Analytical Chemistry

Abstract

Ion packets introduced from gates, ion funnel traps, and other conventional ion injection mechanisms produce ion pulse widths typically around a few milliseconds or less for ion mobility spectrometry (IMS)-based separations on the order of 100 milliseconds. When such ion injection techniques are coupled with ultralong pathlength traveling wave (TW)-based IMS separations (i.e., on the order of seconds) using structures for lossless ion manipulations (SLIM), typically very low ion utilization efficiency is achieved for continuous ion sources (e.g. ESI). Even with the ability to trap and accumulate much larger populations of ions than conventionally feasible over longer time-periods in SLIM devices, the subsequent long separations lead to overall low ion utilization. Here, we report the use of a highly flexible SLIM arrangement enabling concurrent ion accumulation and separation, and achieving near-complete ion utilization with ESI. We characterize the ion accumulation process in SLIM, demonstrate >98% ion utilization, and show both increased signal intensities and measurement throughput. This approach is envisioned to have broad utility to applications e.g. involving the fast detection of trace chemical species. “

2.1.1 Need for Concurrent Accumulation

Ion mobility spectrometry (IMS) is an analytical technique that provides separation of different species based on their ionic mobilities.¹⁻⁵ Ions with different mobilities are separated as they travel in a gas under the influence of an electric field.^{6, 7} Unlike liquid phase separations that typically occur on the order of minutes, IMS-based separations are much faster (typically milliseconds). IMS coupled with mass spectrometry (MS) has become a versatile tool for ion separation, detection, and characterization.⁸⁻¹² A variety of IMS platforms with distinctive capabilities have been developed, such as classical drift tube ion mobility spectrometry (DTIMS),¹³ traveling wave ion mobility spectrometry (TWIMS),^{14, 15} high-field asymmetric ion mobility spectrometry (FAIMS),¹⁶ differential mobility analysis (DMA)¹⁷ and trapped ion mobility spectrometry (TIMS).¹⁸ DTIMS utilizes a constant electric field, and typically low E/N conditions, where ions are separated according to their mobilities, but the ultimate resolution achievable is limited by the maximum voltage drop feasible across the drift tube or length of the drift tube among other factors like injection pulse width, ambient temperature, random diffusion, homogeneity of electric field and coulombic repulsion.^{19, 20} Unlike DTIMS, TWIMS can separate ions with low DC voltages using dynamically varying and repetitive electric fields.²¹ Importantly with TWIMS, the electric potentials required are independent of path length.

Structures for lossless ion manipulations (SLIM), developed at our laboratory,²² is capable of performing TWIMS-based separations. SLIM incorporates two planar surfaces patterned with electrode arrays for ion confinement using radiofrequency (RF) and DC voltages, in conjunction with separations using TW.²³ In SLIM, TW electrodes can be arranged with great flexibility to enable ion turns,²⁴ switches,²⁴ and multi-pass operation to provide unprecedented IMS resolution^{25, 26}, and providing enhanced analytical utility for many applications.^{22, 27} However, the increased resolution with ultralong pathlength separations²⁸ in SLIM IMS-MS incurs longer separation times. Thus, gains due to improvements in IMS resolution may be offset by decreased ion utilization and throughput, and should also be considered in the overall performance evaluation. A typical IMS separation of 10 to 100 ms long typically utilizes a pulse of ions having a temporal width on the scale of 1 ms or less.^{19, 29, 30} While these ions are being separated no other ion packets are typically introduced, resulting in an overall low ion utilization. In SLIM this issue is exacerbated due to longer separation times (typically 0.1 to 10 s). The ability to increase the injected ion population size has been enhanced by ion accumulation using ion trapping regions, such as in an ion funnel trap³¹, which has allowed ion populations of 10^6 to 10^7 charges to be accumulated and injected for each separation. Of specific relevance here, 'in-SLIM' ion accumulation has been recently shown to allow the use of much larger ion populations in IMS separations, extending to $>10^9$ charges.^{32, 33} However, ion utilization is still limited due to the sequential nature of the ion accumulation in-SLIM followed by the IMS separation steps. The ions from continuous ion sources are not used during the ion separation time in these systems as ions need to be blocked from entering the device during an ongoing separation.

Some methods have been demonstrated to overcome the limitation. Poltash et al. present a Fourier transform ion mobility coupling with orbitrap mass spectrometer for improved ion transmission and throughput in mismatched duty cycle instruments.³⁴ Other methods to better utilize ions in an IMS experiment that have been developed include

multiplexing.³⁵⁻³⁹ An IMS spectrum which is a composite of separation arising from each packet is then deconvoluted to obtain the true spectrum with improved S/N. However, ion utilization efficiency is still limited (depending on the length of the pseudo-random injection sequence of the multiplexing scheme),⁴⁰ and the data processing (demultiplexing) typically introduces artifacts for low abundance species leading to false negatives in detection upon artifact removal.⁴¹ Further, when SLIM is used in the multi-pass mode, multiplexing is not possible to be used as the multiple ion packets cycling in the system with multiple ion pulses being injected poses an unsurmountable challenge as far as data deconvolution is concerned. A potential solution is to accumulate ions while a separation is ongoing (instead of discarding the ions) and use the accumulated ions for performing the subsequent run of the experiment.

Some researchers have used additional ion trapping devices to accumulate ions upstream of the IMS.^{15, 42, 43} Parallel accumulation of ions in IMS during analysis was also demonstrated in a TIMS/TIMS instrument,⁴⁴ with near 100% duty cycle by using a gas flow and counter electric field to trap and accumulate ions. A gas flow with a counter electric field was used to accumulate ions, followed by the release of ions for TIMS analysis. The use of parallel accumulation enabled close to 100% duty cycle being reported. Detailed characterization of the accumulation time, resolving power, peak intensity were discussed. While, use of gas flow and counter electric fields are conducive for parallel accumulation in the linear arrangement of electrodes as in TIMS, in the serpentine arrangement of SLIM the use of gas flows is not preferred. Also, the reported TIMS experiment showed accumulation times of up to 0.1s. However, SLIM performs separations over extended times over a second and thus requires significantly large ion accumulation capacity to achieve a 100% duty cycle. This can be accomplished in SLIM using a traveling wave and a counter DC voltage to accumulate ions. Additionally, SLIM provides flexibility in the electrode arrangement, dynamic control of voltages, and the ability to design the board layout to execute complex ion motion for an extended length of time. Here, we report on a new TW-SLIM module with decoupled accumulation and separation regions, which enables the IMS separation with multi-pass capabilities to be performed concurrently with ion accumulation over times-scales of seconds. Thus an overall high ion utilization efficiency is obtained. This in-SLIM concurrent accumulation method is shown to achieve >90% overall ion utilization efficiency of ions introduced from a continuous source (ESI) while maintaining SLIM ion manipulation capabilities.

2.1.2 Methods

Materials

Lipid	Formula	[M-H] ⁻	^{DT} CCS _{N2} (Å ²)	Concentration (μM)
PE Lyso 14:0	C ₁₉ H ₄₀ NO ₇ P	424.2	203.4	5
PS Lyso 16:0	C ₂₄ H ₅₀ NO ₇ P	496.3	221.3	5
PE 12:0/12:0	C ₂₉ H ₅₈ NO ₈ P	578.4	240.3	5
PG 14:0/14:0	C ₃₄ H ₆₆ O ₁₀ PNa	665.4	259.2	2

PG 17:0/17:0	C ₄₀ H ₇₈ O ₁₀ PNa	749.5	278.0	2
PS 18:0/18:0	C ₄₂ H ₈₁ NO ₁₀ PNa	790.6	289.4	5
PG cis 18:1/18:1	C ₄₂ H ₇₈ O ₁₀ PNa	773.5	281.5	2
PG trans 18:1/18:1	C ₄₂ H ₇₈ O ₁₀ PNa	773.5	284.5	2

ESI-L low concentration Agilent tuning mixture (hexakis-(fluoroalkoxy)phosphazines, HFAP, Agilent Technologies, Santa Clara, CA) was diluted to half the concentration of the standard solution. 8 phospholipids (Avanti Polar Lipids, Alabaster, AL) were dissolved in methanol to prepare lipid mixtures for analysis. (Table 1)

Table 1. Phospholipids used in this work

The SLIM IMS-MS Platform

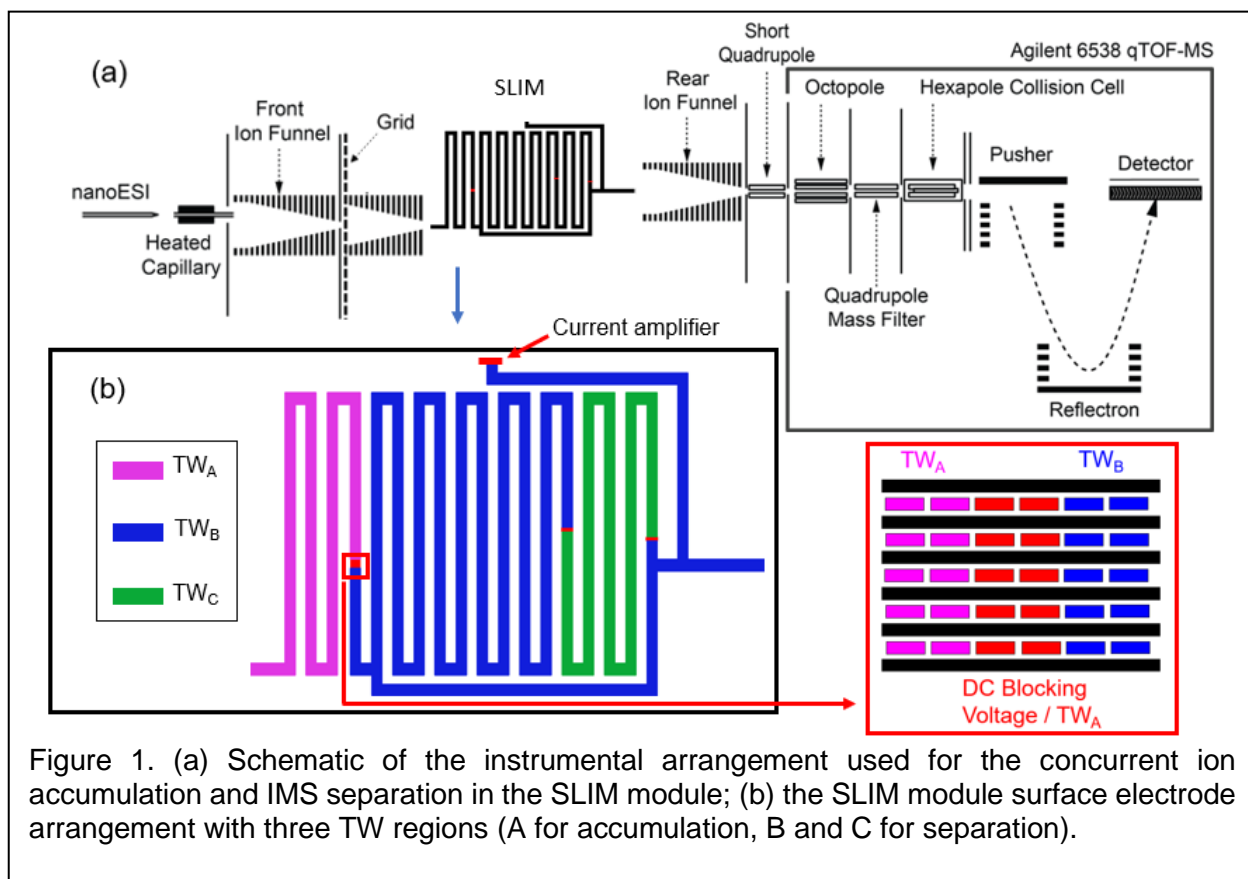


Figure 1. (a) Schematic of the instrumental arrangement used for the concurrent ion accumulation and IMS separation in the SLIM module; (b) the SLIM module surface electrode arrangement with three TW regions (A for accumulation, B and C for separation).

Figure 1a shows the schematic of the SLIM IMS-MS instrument used in this work. A nanoelectrospray ionization source connected to a syringe pump (Hamilton Company, Reno, NV) with a flow rate of 0.5 $\mu\text{L}/\text{min}$ in negative ion mode (-3000 V) was used for generating gas-phase ions. The ions were sampled into the SLIM-MS system using a heated capillary inlet (biased to -390 V). The current generated by the source was measured at this capillary interface and was found to be 10 (± 0.7) nA. Two pumping

stages were used after the capillary. The first stage housed an ion funnel (at ~ 3 Torr N_2), which was connected to a second pressure region through a conductance limiting orifice (2.5 mm i.d.) housing a second funnel followed by the SLIM. The two funnels carried opposite phase RF voltages on adjacent electrodes to provide ion confinement and focusing. The adjacent ring electrodes of the funnels additionally carried DC voltages across a resistor chain. The front funnel had a voltage drop from -380 V to -230 V. The second funnel had a voltage drop from -225 V to -150 V. The electric field strength in both the funnels was approximately 20 V/cm. A conductive grid between the front ion funnel and the second funnel was electrically biased to transmit ions (by applying a voltage of -227 V) or block ions (+20 V). The second funnel was interfaced with SLIM, which was floated at -140 V. The ions transmitted through the two funnels arrive at the entrance of the SLIM, where a current of 0.6 nA was measured at the SLIM entrance. The SLIM had a serpentine arrangement of electrodes providing a nominal path length of 10 m. The pressure in the SLIM housing was maintained at ~ 0.1 Torr above the first funnel region to provide a positive pressure differential and minimize contamination (e.g. neutrals and charged large particles) of the SLIM. The SLIM ion path exited to a rear ion funnel which was connected to a time-of-flight mass spectrometer (Agilent 6538, Agilent, Santa Clara, USA) across a pressure-limiting orifice at the end of the back funnel and a short quadrupole.

Figure 1b shows the detailed layout of the 10-meter SLIM platform that was used. DC guard voltage (-12V) and RF potentials (280 V_{p-p}) with 1.04 MHz frequency were used for ion confinement. TW_A amplitude was varied between 5 V to 40 V. TW_B and TW_C were maintained at 40 V for surfing conditions and 15 V for separation conditions. The TW speed in all the regions of the SLIM board was 64 m/s (electrode-to-electrode voltage stepping frequency of 8.0 kHz) (Voltage details are shown in Table S1 – 6). As previously reported, all the regions of the SLIM contain 6 strips of electrodes supplied with an alternating opposite phase of RF voltage.^{28, 33, 45-50} The RF electrodes are interspersed with TW electrodes. Three distinct regions were incorporated into this SLIM platform, each supplied with distinctly controlled TW. TW_A region (pink color in Figure 1b) is the ion accumulation region (2 m), which is supplied with a TW profile optimized for gentle and extended time ion accumulation. TW_A region ends with two blocking electrodes (represented in color red) which alternate between a DC voltage and TW profile depending on whether ions are being accumulated or ejected (i.e. transferred to the TW_B region). TW_B (color blue in Figure 1b) is the ion separation region (5.2 m), which is supplied with a TW profile to perform IMS separations. TW_C (the color green in Figure 1b) is supplied with either the same TW as TW_B in this paper or a distinct profile in the future work.^{25, 32, 51} At the end of the TW_C , another additional ion switch enables ions (or a selected range of mobilities) to be re-routed to a Faraday plate connected to a current amplifier (Keithley 428, Keithley Instruments Solon, OH), that is referenced to 0 Volts, to measure the current. At the end of the TW_C region, the SLIM transitions to a TW_B section and is followed by a switch region where ions can be sent to the exit of the SLIM or back the beginning of TW_B for additional passes; i.e. a multi-pass arrangement. Importantly, this arrangement does not utilize the TW_A region, which enables an in-SLIM ion accumulation while a multi-pass separation is being executed.

2.1.3 Results and Discussion

As shown in Figure 1b, the TW_A interfaces with the TW_B region through the presence of two independently controlled electrodes between them. The independent electrodes enable the application of either a DC potential normal TW. When DC potential is applied, a barrier is created for TW_A preventing them from reaching TW_B , allowing ion accumulation. When TW_A is applied to the independent electrodes, ions are injected from to TW_B . Figure 2a shows the electric potential surface diagram the interface when a blocking voltage is to be applied. The ions generated from the ion source through the TW_A region towards TW_B region. At the interface, the blocking voltage prevents the ions moving into the TW_B region. The remain confined in the TW_A region are unevenly distributed in the that keeps pushing ions towards interface but are prevented from forward by the blocking voltage. understand the distribution of ions interface blocking region between and TW_B , ions accumulated at region were transported in surfing to the detector. During the accumulation time the TW_A amplitude was constant (5 V) and blocking voltage was -50 V and - on the two DC electrodes at the interface. Subsequent to the ion accumulation step, the ions were injected into TW_B region. The injection step was accomplished switching the voltage in TW_A to 40 V, and replacing the blocking voltages on the two independent electrodes with TW_A . The regions TW_B and TW_C were maintained at constant voltage amplitudes of 40 V throughout the process. Since the ions moved under surfing conditions, the arrival time distribution of the ions obtained here represented the

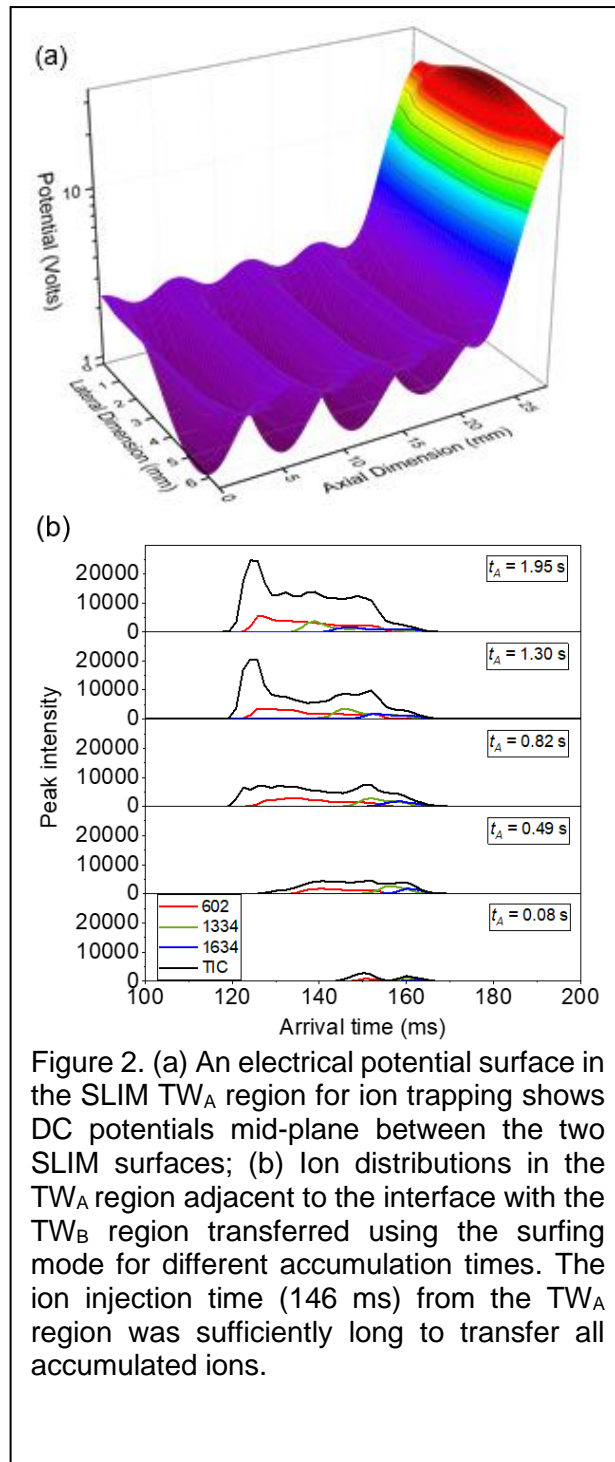


Figure 2. (a) An electrical potential surface in the SLIM TW_A region for ion trapping shows DC potentials mid-plane between the two SLIM surfaces; (b) Ion distributions in the TW_A region adjacent to the interface with the TW_B region transferred using the surfing mode for different accumulation times. The ion injection time (146 ms) from the TW_A region was sufficiently long to transfer all accumulated ions.

region
or a
ions in
 TW_A
near
move
the
from
ions
and
 TW_A
the
going
To
at the
 TW_A
 TW_A
mode
the
80 V
by

ion packet width that was accumulated in the TW_A region. Figure 2b shows the overall distribution profiles for a range of ion accumulation times (for a sample of phosphazine ions). As expected, the accumulated ion intensities increased with increased accumulation time. The observed distributions show a peak at earlier arrival time followed by a relatively more uniform accumulation packet distribution. The initial peak corresponds to the concentration of ions as TW_A pushes ions against the blocking voltage. Beyond a certain limit, it can be presumed that the later arriving ions will be screened from arriving at the interface region due to the already accumulated ion packet, thus accumulating them progressively behind the interface region. In this way the while TW_A region could be accumulated with in-coming ions over time. The Figure 2b also shows individual mass traces of the accumulated ion packets. The mass distribution associated with the accumulated packet indicates that the accumulated ions have some pre-separation in the TW_A region. Thus, the effective width of individual peaks is somewhat narrower than the width of the overall packet. This pre-separation process (potentially arising due to ions being pushed against the blocking voltages with the TW , some reorganization of the peaks due to coulombic effects as they build-up at the interface, the faster ions arriving at the interface and screening the lower mobilities from reaching the interface) is an important piece of study which will affect the eventual peak widths of the separation, which are the subject of a separate study in the future. The accumulated ion packets were routed to the current measurement electrode (near the end of SLIM and prior to exit to MS) to know the total number of ions accumulated. For example, at the accumulation time $t_A = 1.95$ s, a current of 23.4 pA was measured, which corresponded to 1.5×10^8 accumulated ions.

The number of ions accumulated and thus the ultimate signal intensity is also effected by the TW_A amplitude. To study these effects, the TW_A amplitude was varied from 5 V to 15 V with varied accumulation time (Figure 3a-c) and the signal intensity of each ion was measured. A blocking voltage of -50 V and -80 V was applied to the two blocking electrodes at the TW_A/TW_B interface to operate the ion accumulation process. The timing tables for the following experiments have been detailed in the Supplementary Information (Table S1 - 6).

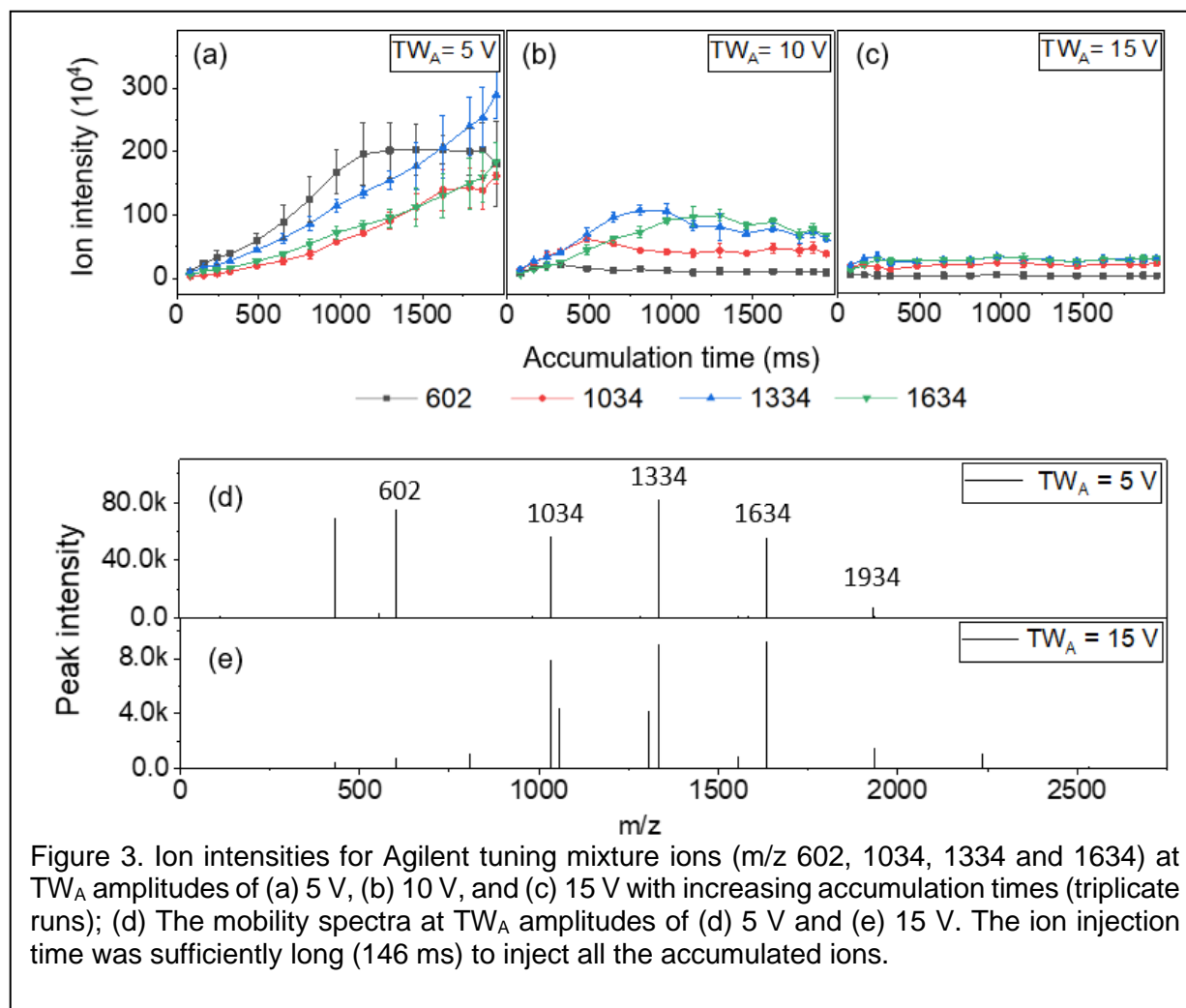


Figure 3. Ion intensities for Agilent tuning mixture ions (m/z 602, 1034, 1334 and 1634) at TW_A amplitudes of (a) 5 V, (b) 10 V, and (c) 15 V with increasing accumulation times (triplicate runs); (d) The mobility spectra at TW_A amplitudes of (d) 5 V and (e) 15 V. The ion injection time was sufficiently long (146 ms) to inject all the accumulated ions.

Signal intensity of accumulated ions increased with increased accumulation time, still a point where the ion population accumulated plateaued at a saturation point. However, the increase was more pronounced at lower TW_A amplitudes. At lower TW_A voltages, the time to arrive at the evident 'saturation' point for ion accumulation is larger (for example, at 10 V, the saturation is reached at around 1 s, whereas at 5 V showed several species experienced continued increases extending to >2 s). This increased ability to hold ions at lower TW_A voltages can be attributed to a more gentle 'push' of ions towards the accumulation barrier. Thus, ions have more freedom rollover the TW and redistribute without being pushed against the interface barrier. A higher TW_A region voltage during

accumulation leads to decreased ion accumulation. Also, higher TW_A conditions could lead to undesirable ion losses and potential activation at the interface. The mass spectra at lower TW_A voltage (5 V) and higher voltage (15 V) were compared (Figure 3d and 3e). The use of lower TW_A voltages does not result in significant ion activation of phosphazine ions, but ion losses and potential fragmentation are seen at 15 V amplitude.

While ions can be accumulated for seconds in the current SLIM configuration, as discussed before, involves injecting a small packet of into the separation region. All the accumulated ions need to exit the region and be injected into TW_B in shortest possible time. This injection process involved (as alluded to previously) modulating voltages applied to TW_A , upstream electrode, and the TW_A/TW_B interface blocking voltages. The diagram for this is shown in Figure 4. The TW_A , TW_B and TW_C were synchronized to the same clock, the TW_A was a normal TW. To enable injecting ions into TW_B , the injection conditions were held for a certain injection time (t_{inj}) to allow injection of all ions to the separation region. Ions were injected to TW_B most quickly under surfing conditions (by increasing TW_A to 40 V). This could either be instantaneously or by ramping the voltage from 5 V to 40 V at a fixed rate. The benefit of the later approach that the ion packet injection process became gentler particularly for some fragile molecules. As will be discussed subsequently, some of the accumulation experiments with lipid samples require ramping to prevent ion losses that occurred by instantaneous change from 5 to 40 V (see Supplementary Information Figure S1). To inject ions for IMS separation, a ramping rate of 0.7 V/ms was used in the TW_A region, in an experiment to characterize the ion injection into TW_B . In addition to TW_A , the blocking voltage was lowered during t_{inj} to TW voltages and the upstream grid was raised to prevent ions entering the SLIM region. Closing the grid (black line in Figure 4a) prevented ions from entering the SLIM during the transfer of accumulated ions to the TW_B region. Once ions were injected for a predetermined injection time (t_{inj}), the blocking voltage between TW_A/TW_B was raised to again block ions, and the TW_A amplitude dropped to a lower

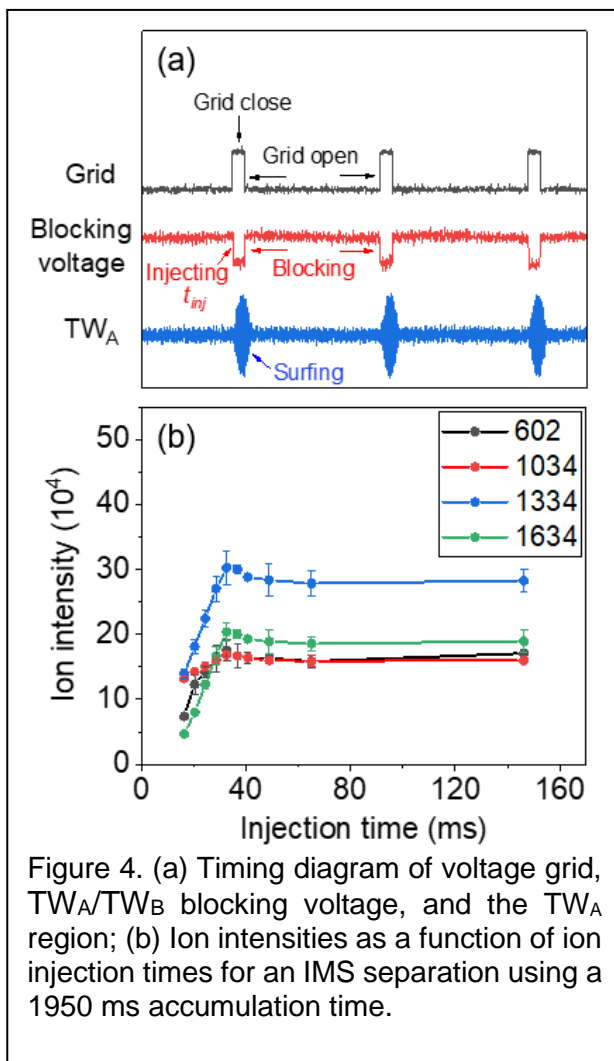


Figure 4. (a) Timing diagram of voltage grid, TW_A/TW_B blocking voltage, and the TW_A region; (b) Ion intensities as a function of ion injection times for an IMS separation using a 1950 ms accumulation time.

a few

IMS
ions

TW_A
the

briefly
the
grid

timing
4a.

and

the

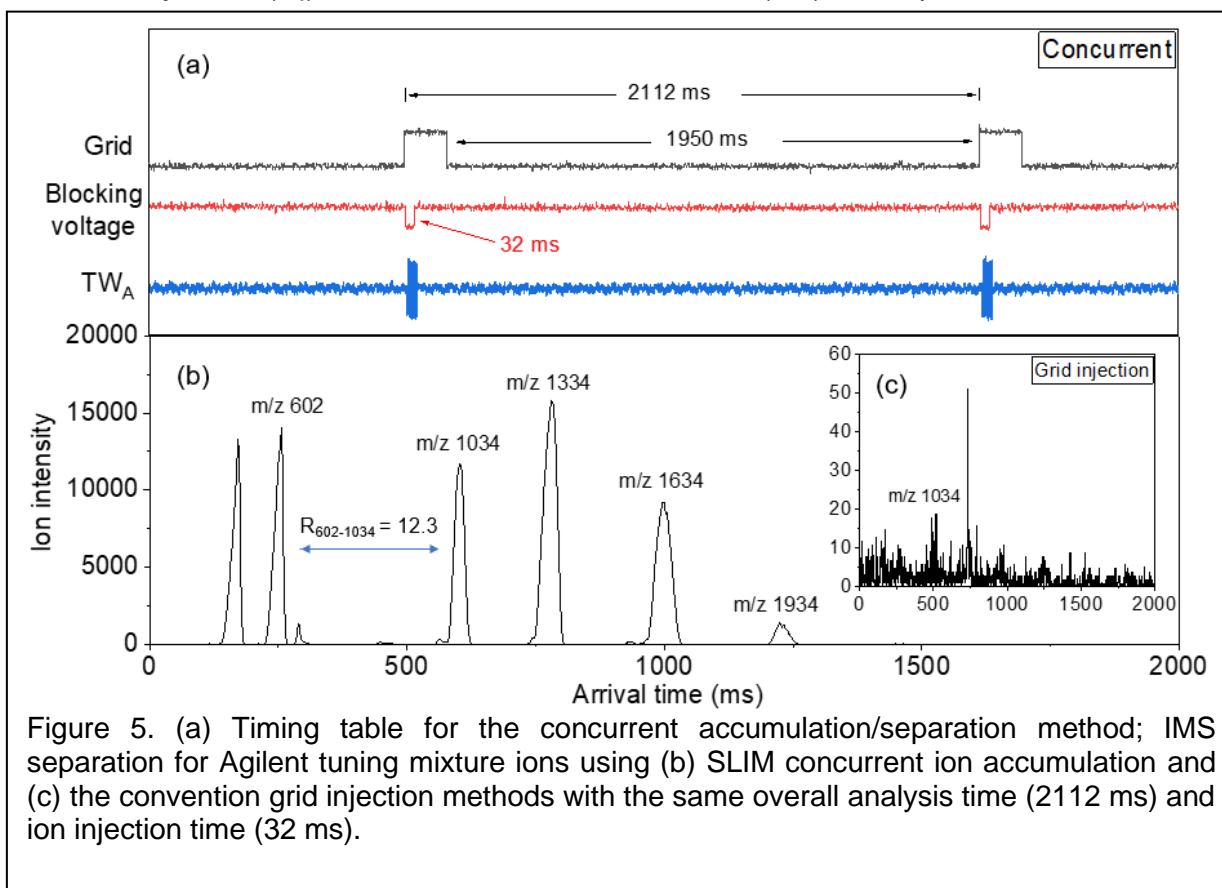
the
done

rate.
was

voltage suitable for accumulation and followed by lowering the voltage of the grid to begin ion accumulation for the next cycle. One injection followed by separation and detection constitutes an accumulation cycle. Multiple such cycles may be executed and averaged for improved S/N. Unless otherwise mentioned, we averaged over 10 cycles.

To initially determine the time needed to completely transfer ions before the next accumulation period, the ion intensities were recorded as a function of t_{inj} . As shown in Figure 4a, the blocking voltage (red) was dropped at the beginning of one separation period to transfer the ions accumulated during the previous separation window, and the TW_A amplitude (blue) was simultaneously ramped to that used for surfing (40 V) to accomplish fast ion transfer. We note that the grid (black) was 'closed' to prevent ions from entering the accumulation region during the ion transfer period in this work, although this small period where ions were discarded is not strictly required. Thus, after ion injection, the ions were separated in the TW_B/TW_C regions, while the TW_A/TW_B blocking voltage was set to high. Figure 4b shows the signal intensities for different injection times (t_{inj}). As can be seen, all the ions over a wide mass range (i.e. m/z 602 to 1634) were effectively injected within 32 ms. (The data and error bars are based upon 10 accumulation events.) Injection times shorter than 32 ms were insufficient for all ions to transfer into the TW_B region, but injection times longer than 32 ms allowed essentially all ions accumulated over several seconds to be transferred. Ions are spread over several meters of the TW_A region (from the SLIM entrance to the TW_A/TW_B interface) over the time of ion accumulation (seconds). Here, for the 2 m long accumulation region in TW_A , we were able to allow up to 2 s of accumulation time. If the length of this were to be increased, the accumulation time could be higher due to increased charge carrying capacity of the longer region. The shorter regions lead to less accumulation time. This is so because the ion packets occupy a certain spatial span in the TW_A region. We need ~ 30 ms to exit all ions from TW_A at 64 m/s. Thus, the width of the ion accumulation packet which is surfing is about $64 \text{ (m/s)} \times 32 \text{ (ms)} = \sim 2 \text{ m}$. Thus, the accumulated packet fully spanned the TW_A region. This phenomenon can be exploited to allow extended ion accumulation times with simultaneously short ion transfer times between the TW_A and TW_B regions, resulting in increased ion utilization efficiency. If the ion transfer time is a small fraction of the total separation time, or ion introduction can be maintained during the separation step (as noted above), high ion utilization efficiencies can be achieved.

Consistent with the previous discussion, we define the ion utilization efficiency (η) here as the ratio of the time for which ions are utilized for the analysis over the total time of the analysis. In the case of a grid used to pulse a small packet of ions (i.e. without ion accumulation), the $\eta_{grid} = \frac{t_{inj}}{t_{inj}+t_{sep}}$. Here, t_{tot} is the total analysis time per a single acquisition, t_{inj} is the time for injection and t_{sep} is the time for separation. The net ion utilization with accumulation is defined as the ratio of the time of accumulation over the total analysis time (t_{tot}) that comprises the time for separation (t_{sep}), the time for ion transfer or injection (t_{inj}), and time for ion accumulation (t_{acc}). Most previous SLIM studies

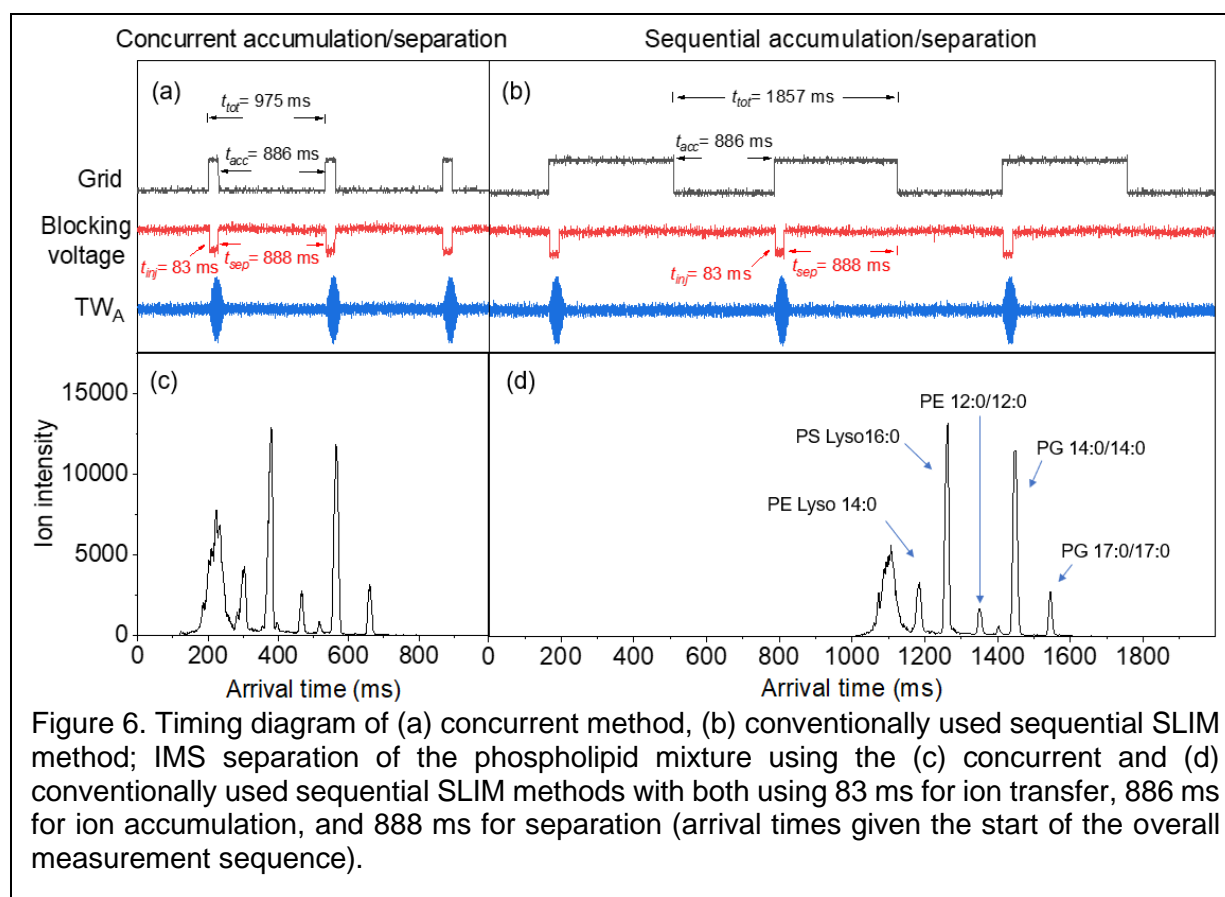


have been performed using sequential ion accumulation and ion separation steps. After accumulation, a new experiment cycle then begins with fresh ion accumulation, thus providing an $\eta_{SLIM_seq} = \frac{t_{acc}}{t_{acc}+t_{inj}+t_{sep}}$. In comparison, when using the SLIM design as described here (Figure 1) we are able to concurrently accumulate ions while separation is ongoing providing an efficiency $\eta_{SLIM_conc} = \frac{t_{acc}}{t_{inj}+t_{sep}}$. Any other losses, e.g. due to space charge or storage capacity of the SLIM, will obviously reduce the overall ion utilization efficiency.

The timing diagram for concurrent accumulation and separation is shown in Figure 5a. With this method, ions were accumulated for 1950 ms with 100% ion accumulation efficiency (i.e. without losses, as indicated by the linear increase in ion current with t_{acc} as shown in Figure 3a) and transferred between regions in 32 ms. The t_{tot} of 2112 ms

corresponds to 92.3% ion utilization efficiency. It is instructive to compare the present performance achievable, with that obtained using conventional ion injection (i.e., using the external grid 'shutter' with no ion accumulation, where we achieve the traditionally low ion utilization with IMS). This can be compared to the conventional grid injection (32 ms) with the same analysis time of 2112 ms, which results in an utilization efficiency of 1.5%. The ion intensity of grid injection can be increased by increasing the injection time, however, longer injection times will significantly broaden peak widths. These IMS separations are shown in Figure 5b and 5c, and indicate a significant improvement in signal intensities and ion utilization based upon the use of concurrent accumulation in SLIM. The ion utilization efficiency increased by ~60 times. In addition, the signal intensity and signal-to-noise (S/N) of peaks increased dramatically. For example, the signal intensity of m/z 1034 in Figure 5c using a simple grid injection was 20 a.u. (with a S/N of 4). Whereas by using the concurrent accumulation process, the signal intensity improved to 12500 a.u. (S/N = ~2118) enabling an improvement of signal intensity by ~625-fold times with concurrent accumulation compared to grid injection.

In our previous multi-pass SLIM designs^{22, 25, 28}, the ion path moves the ions from the end of the SLIM to close to the starting point of the ion path, to maximize ion path length executed in the multiple passes. However, this prevents ion accumulation as long as a separation is ongoing. In the SLIM design reported here, the return path connects to the TW_B region, allowing operation of the TW_A ion accumulation region to be independent of



the TW_B separation region. This in-SLIM accumulation feature also eliminates the need for an upstream ion funnel trap⁵² for external ion accumulation.

The concurrent accumulation with separation increases both ion utilization efficiency and

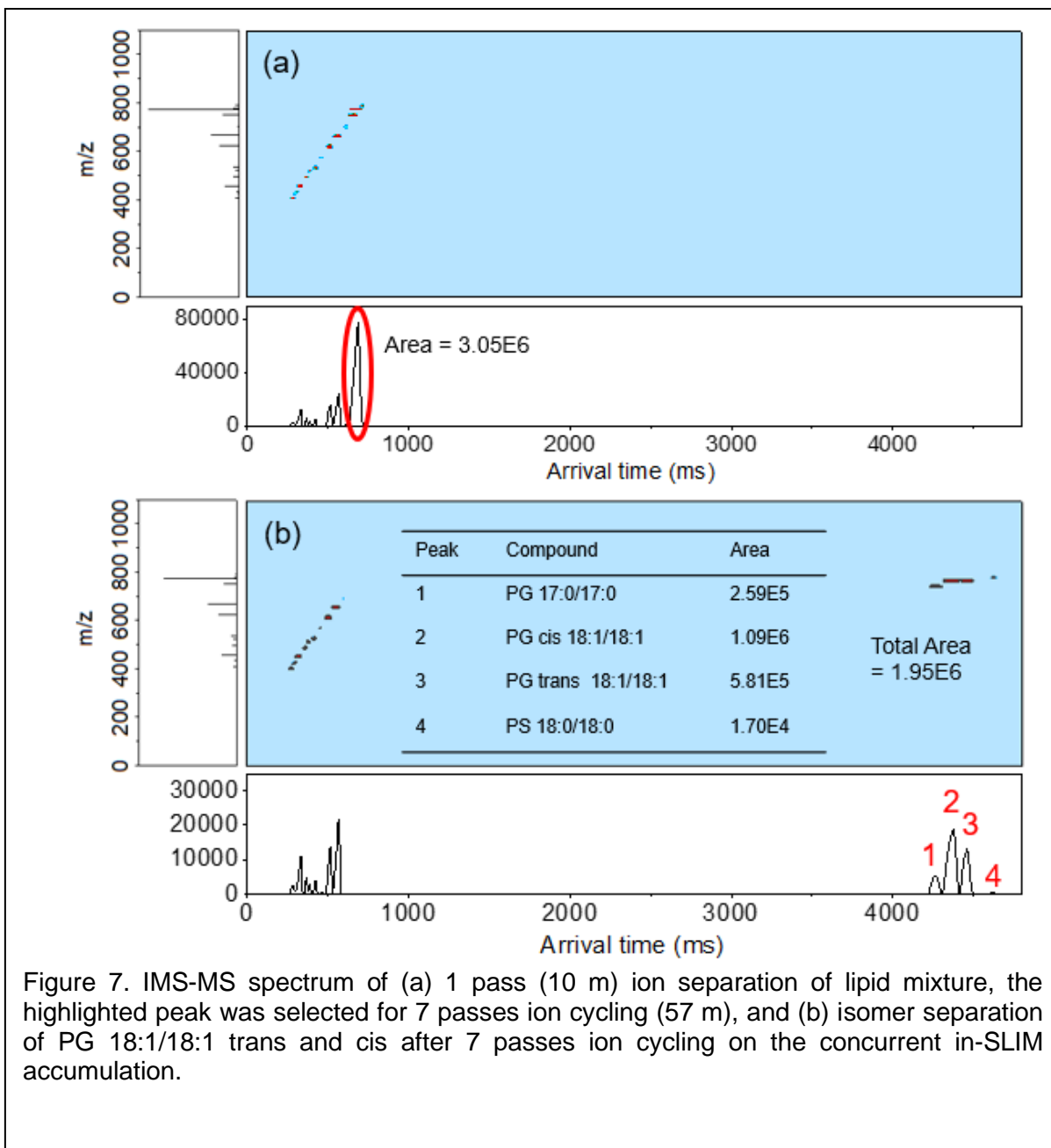


Figure 7. IMS-MS spectrum of (a) 1 pass (10 m) ion separation of lipid mixture, the highlighted peak was selected for 7 passes ion cycling (57 m), and (b) isomer separation of PG 18:1/18:1 trans and cis after 7 passes ion cycling on the concurrent in-SLIM accumulation.

throughput (i.e. separation acquisition rate). Figure 6 shows a comparison between the concurrent accumulation/separation and sequential accumulation/separation in SLIM. In the concurrent accumulation (Figure 6a), a single signal acquisition event in this case is 975 ms long. The signal acquisition step begins with the injecting of ions into the TW_B region from the TW_A region (for 83 ms here). During this time, the grid set high to block the ions going into the SLIM. After the ion injection, the blocking voltage between the $TW_{A/B}$ interface is back on and the TW_A amplitude is dropped to enable accumulation of

ions in TW_A region (for 886 ms here). During this time the ions injected are undergoing separation in TW_B and TW_C . After the 886 ms, the separation is completed, grid is closed in preparation for the next injection. The analysis time of one IM separation at concurrent and the sequential SLIM operation are 975 ms and 1857 ms, respectively, to present the same signal intensity, demonstrating an improved throughput and speed of analysis using the concurrent accumulation method. A nearly two times increase in the analysis speed is observed compared to the traditional sequential accumulation approach with all other SLIM operational parameters being the same. We note that in the current design linear range of accumulation extends over ~ 2 s. Beyond 2s of accumulation time, we presume that excessive ion populations and the finite charge trapping capacity of SLIM would lead to decreased accumulation efficiency of the ions.

Concurrent ion accumulation and separation processes are particularly advantageous in multi-pass SLIM IMS measurements. As an example, two phospholipid isomers to be separated from a lipid mixture using SLIM in a single 10 m pass are shown in Figure 7a. As can be seen, a peak containing two isomers (PG 18:1/18:1 trans and cis) was the main peak. This peak was then selected for multiple passes using the ion switch while the rest of the ions were sent to the MS for detection. The single-pass operation has a separation time less than a second, whereas 7 passes (57 m) were needed to completely separate the components of the selected peak. This would originally have constituted a loss of duty cycle/ion utilization efficiency if a sequential ion accumulation/separation experiment was performed. However, we were able to achieve high utilization efficiencies ($\sim 98.2\%$, $t_{acc} = 4750$ ms $t_{tot} = 4840$ ms) with concurrent accumulation. At the end of the separation, the two PG isomers (No. 2 and 3) were separated with a full width at half maximum (FWHM) resolution of 1.56 after 7 passes. Two small peaks (No. 1 and 4), close to the two isomer peaks with very similar collision cross sections (CCS), were also observed, which were identified as PG 17:0/17:0 (~ 4260 ms) and PS 18:0/18:0 (~ 4620 ms). We also compared the peak area of the single peak in the single pass and multi-pass measurements and found the total peak areas of the four components were similar after 7 passes. A total peak area of the four resolved peaks in the 7-pass separation is obtained at 1.95×10^6 , which is comparable to that of the parent ion at 3.05×10^6 in the single pass run, demonstrating the high-resolution separation with concurrent in-SLIM ion accumulation.

2.1.4 Overall Utility

This work has shown significant improvements to the performance of IMS-MS in terms of ion utilization efficiency, and the resultant impacts on speed and sensitivity are major factors driving instrumental design and development. These gains are based upon a novel TW-based SLIM platform with concurrent ion accumulation and separation, improving ion utilization efficiency with continuous ion sources to nearly 100%. The approach exploits the capability of SLIM to trap and accumulate much larger ion populations than feasible with conventional platforms. Investigations on the effect of TW amplitude to the ion accumulation revealed the preference of lower TW amplitude (5 V) for gentle accumulation. The signal intensities resulting from the ion populations with the concurrent accumulation approach in SLIM are shown to be as much as ~ 625 -fold greater than using a conventional grid injection approach. In contrast to the sequential

accumulation/separation of the previous SLIM designs, the concurrent accumulation and IMS separation decreases the overall analysis time (i.e. the spectrum acquisition rate) while increasing the ion utilization efficiency. This provides the same signal intensities in approximately half the analysis time and doubling the measurement throughput compared to the previous SLIM design. Additionally, the multi-pass ion manipulation feature with the concurrent accumulation SLIM, demonstrated with baseline separation of lipid isomers, maintains the capability for high-resolution IMS separations. This manuscript has been submitted and is in final review with ACS Analytical Chemistry. It describes the development of a system that can perform IMS/MS analysis with ~100% ion utilization efficiency. This development allows scaling up of the material deposited via IMS/MS selectivity to quantities that are amenable for characterization using other analytical techniques.

References

- Gabelica, V.; Marklund, E., Fundamentals of ion mobility spectrometry. *Current Opinion in Chemical Biology* **2018**, *42*, 51-59.
- Cumeras, R.; Figueras, E.; Davis, C. E.; Baumbach, J. I.; Gràcia, I., Review on Ion Mobility Spectrometry. Part 1: current instrumentation. *Analyst* **2015**, *140* (5), 1376-1390.
- Zucker, S. M.; Lee, S.; Webber, N.; Valentine, S. J.; Reilly, J. P.; Clemmer, D. E., An ion mobility/ion trap/photodissociation instrument for characterization of ion structure. *J Am Soc Mass Spectrom* **2011**, *22* (9), 1477-85.
- Groessl, M.; Graf, S.; Knochenmuss, R., High resolution ion mobility-mass spectrometry for separation and identification of isomeric lipids. *Analyst* **2015**, *140* (20), 6904-6911.
- Wu, C.; Siems, W. F.; Klasmeier, J.; Hill, H. H., Separation of Isomeric Peptides Using Electrospray Ionization/High-Resolution Ion Mobility Spectrometry. *Analytical Chemistry* **2000**, *72* (2), 391-395.
- Mason, E. A.; McDaniel, E. W., Transport properties of ions in gases. *NASA STI/Recon Technical Report A* **1988**, *89*, 15174.
- Viehland, L. A.; Guevremontb, R.; Purves, R. W.; Barnett, D. A., Comparison of high-field ion mobility obtained from drift tubes and a FAIMS apparatus. *International Journal of Mass Spectrometry* **2000**, *197* (1), 123-130.
- Plasencia, M. D.; Isailovic, D.; Merenbloom, S. I.; Mechref, Y.; Clemmer, D. E., Resolving and assigning N-linked glycan structural isomers from ovalbumin by IMS-MS. *Journal of the American Society for Mass Spectrometry* **2008**, *19* (11), 1706-1715.
- Kloniecki, M.; Jablonowska, A.; Poznański, J.; Langridge, J.; Hughes, C.; Campuzano, I.; Giles, K.; Dadlez, M., Ion Mobility Separation Coupled with MS Detects Two Structural States of Alzheimer's Disease A β 1-40 Peptide Oligomers. *Journal of Molecular Biology* **2011**, *407* (1), 110-124.
- Lanucara, F.; Holman, S. W.; Gray, C. J.; Evers, C. E., The power of ion mobility-mass spectrometry for structural characterization and the study of conformational dynamics. *Nature Chemistry* **2014**, *6* (4), 281-294.
- Paglia, G.; Astarita, G., Metabolomics and lipidomics using traveling-wave ion mobility mass spectrometry. *Nature Protocols* **2017**, *12* (4), 797-813.
- Hofmann, J.; Pagel, K., Glycan Analysis by Ion Mobility–Mass Spectrometry. *Angewandte Chemie International Edition* **2017**, *56* (29), 8342-8349.
- Borsdorf, H.; Eiceman, G. A., Ion Mobility Spectrometry: Principles and Applications. *Applied Spectroscopy Reviews* **2006**, *41* (4), 323-375.
- Shvartsburg, A. A.; Smith, R. D., Fundamentals of Traveling Wave Ion Mobility Spectrometry. *Analytical Chemistry* **2008**, *80* (24), 9689-9699.
- Pringle, S. D.; Giles, K.; Wildgoose, J. L.; Williams, J. P.; Slade, S. E.; Thalassinos, K.; Bateman, R. H.; Bowers, M. T.; Scrivens, J. H., An investigation of the mobility separation of some peptide and protein ions using a new hybrid quadrupole/travelling wave IMS/oa-ToF instrument. *International Journal of Mass Spectrometry* **2007**, *261* (1), 1-12.
- Guevremont, R., High-field asymmetric waveform ion mobility spectrometry: A new tool for mass spectrometry. *Journal of Chromatography A* **2004**, *1058* (1), 3-19.
- de la Mora, J. F.; de Juan, L.; Eichler, T.; Rosell, J., Differential mobility analysis of molecular ions and nanometer particles. *TrAC Trends in Analytical Chemistry* **1998**, *17* (6), 328-339.
- Michelmann, K.; Silveira, J. A.; Ridgeway, M. E.; Park, M. A., Fundamentals of Trapped Ion Mobility Spectrometry. *Journal of the American Society for Mass Spectrometry* **2015**, *26* (1), 14-24.
- Dugourd, P.; Hudgins, R. R.; Clemmer, D. E.; Jarrold, M. F., High-resolution ion mobility measurements. *Review of Scientific Instruments* **1997**, *68* (2), 1122-1129.
- Bohrer, B. C.; Merenbloom, S. I.; Koeniger, S. L.; Hilderbrand, A. E.; Clemmer, D. E., Biomolecule Analysis by Ion Mobility Spectrometry. *Annual Review of Analytical Chemistry* **2008**, *1* (1), 293-327.
- Giles, K.; Pringle, S. D.; Worthington, K. R.; Little, D.; Wildgoose, J. L.; Bateman, R. H., Applications of a travelling wave-based radio-frequency-only stacked ring ion guide. *Rapid Communications in Mass Spectrometry* **2004**, *18* (20), 2401-2414.
- Ibrahim, Y. M.; Hamid, A. M.; Deng, L.; Garimella, S. V. B.; Webb, I. K.; Baker, E. S.; Smith, R. D., New frontiers for mass spectrometry based upon structures for lossless ion manipulations. *Analyst* **2017**, *142* (7), 1010-1021.

23. Hamid, A. M.; Ibrahim, Y. M.; Garimella, S. V. B.; Webb, I. K.; Deng, L.; Chen, T.-C.; Anderson, G. A.; Prost, S. A.; Norheim, R. V.; Tolmachev, A. V.; Smith, R. D., Characterization of Traveling Wave Ion Mobility Separations in Structures for Lossless Ion Manipulations. *Analytical Chemistry* **2015**, *87* (22), 11301-11308.
24. Garimella, S. V. B.; Ibrahim, Y. M.; Webb, I. K.; Ipsen, A. B.; Chen, T.-C.; Tolmachev, A. V.; Baker, E. S.; Anderson, G. A.; Smith, R. D., Ion manipulations in structures for lossless ion manipulations (SLIM): computational evaluation of a 90° turn and a switch. *Analyst* **2015**, *140* (20), 6845-6852.
25. Deng, L.; Ibrahim, Y. M.; Hamid, A. M.; Garimella, S. V. B.; Webb, I. K.; Zheng, X.; Prost, S. A.; Sandoval, J. A.; Norheim, R. V.; Anderson, G. A.; Tolmachev, A. V.; Baker, E. S.; Smith, R. D., Ultra-High Resolution Ion Mobility Separations Utilizing Traveling Waves in a 13 m Serpentine Path Length Structures for Lossless Ion Manipulations Module. *Analytical Chemistry* **2016**, *88* (18), 8957-8964.
26. Deng, L.; Ibrahim, Y. M.; Baker, E. S.; Aly, N. A.; Hamid, A. M.; Zhang, X.; Zheng, X.; Garimella, S. V. B.; Webb, I. K.; Prost, S. A.; Sandoval, J. A.; Norheim, R. V.; Anderson, G. A.; Tolmachev, A. V.; Smith, R. D., Ion Mobility Separations of Isomers based upon Long Path Length Structures for Lossless Ion Manipulations Combined with Mass Spectrometry. *ChemistrySelect* **2016**, *1* (10), 2396-2399.
27. Garimella, S. V. B.; Nagy, G.; Ibrahim, Y. M.; Smith, R. D., Opening new paths for biological applications of ion mobility - Mass spectrometry using structures for lossless ion manipulations. *Trac-Trend Anal Chem* **2019**, *116*, 300-307.
28. Deng, L.; Webb, I. K.; Garimella, S. V. B.; Hamid, A. M.; Zheng, X.; Norheim, R. V.; Prost, S. A.; Anderson, G. A.; Sandoval, J. A.; Baker, E. S.; Ibrahim, Y. M.; Smith, R. D., Serpentine Ultralong Path with Extended Routing (SUPER) High Resolution Traveling Wave Ion Mobility-MS using Structures for Lossless Ion Manipulations. *Analytical Chemistry* **2017**, *89* (8), 4628-4634.
29. Zheng, X.; Dupuis, K. T.; Aly, N. A.; Zhou, Y.; Smith, F. B.; Tang, K.; Smith, R. D.; Baker, E. S., Utilizing ion mobility spectrometry and mass spectrometry for the analysis of polycyclic aromatic hydrocarbons, polychlorinated biphenyls, polybrominated diphenyl ethers and their metabolites. *Analytica Chimica Acta* **2018**, *1037*, 265-273.
30. Kemper, P. R.; Dupuis, N. F.; Bowers, M. T., A new, higher resolution, ion mobility mass spectrometer. *International Journal of Mass Spectrometry* **2009**, *287* (1), 46-57.
31. Clowers, B. H.; Ibrahim, Y. M.; Prior, D. C.; Danielson, W. F.; Belov, M. E.; Smith, R. D., Enhanced Ion Utilization Efficiency Using an Electrodynamic Ion Funnel Trap as an Injection Mechanism for Ion Mobility Spectrometry. *Analytical Chemistry* **2008**, *80* (3), 612-623.
32. Deng, L.; Garimella, S. V. B.; Hamid, A. M.; Webb, I. K.; Attah, I. K.; Norheim, R. V.; Prost, S. A.; Zheng, X.; Sandoval, J. A.; Baker, E. S.; Ibrahim, Y. M.; Smith, R. D., Compression Ratio Ion Mobility Programming (CRIMP) Accumulation and Compression of Billions of Ions for Ion Mobility-Mass Spectrometry Using Traveling Waves in Structures for Lossless Ion Manipulations (SLIM). *Analytical Chemistry* **2017**, *89* (12), 6432-6439.
33. Deng, L.; Ibrahim, Y. M.; Garimella, S. V. B.; Webb, I. K.; Hamid, A. M.; Norheim, R. V.; Prost, S. A.; Sandoval, J. A.; Baker, E. S.; Smith, R. D., Greatly Increasing Trapped Ion Populations for Mobility Separations Using Traveling Waves in Structures for Lossless Ion Manipulations. *Analytical Chemistry* **2016**, *88* (20), 10143-10150.
34. Poltash, M. L.; McCabe, J. W.; Shirzadeh, M.; Laganowsky, A.; Clowers, B. H.; Russell, D. H., Fourier Transform-Ion Mobility-Orbitrap Mass Spectrometer: A Next-Generation Instrument for Native Mass Spectrometry. *Analytical Chemistry* **2018**, *90* (17), 10472-10478.
35. Ibrahim, Y. M.; Garimella, S. V. B.; Prost, S. A.; Wojcik, R.; Norheim, R. V.; Baker, E. S.; Rusyn, I.; Smith, R. D., Development of an Ion Mobility Spectrometry-Orbitrap Mass Spectrometer Platform. *Analytical Chemistry* **2016**, *88* (24), 12152-12160.
36. Harris, G. A.; Kwasnik, M.; Fernández, F. M., Direct Analysis in Real Time Coupled to Multiplexed Drift Tube Ion Mobility Spectrometry for Detecting Toxic Chemicals. *Analytical Chemistry* **2011**, *83* (6), 1908-1915.
37. Szumilas, A. W.; Ray, S. J.; Hieftje, G. M., Hadamard Transform Ion Mobility Spectrometry. *Analytical Chemistry* **2006**, *78* (13), 4474-4481.
38. Reinecke, T.; Davis, A. L.; Clowers, B. H., Determination of Gas-Phase Ion Mobility Coefficients Using Voltage Sweep Multiplexing. *Journal of The American Society for Mass Spectrometry* **2019**, *30* (6), 977-986.
39. Hong, Y.; Huang, C.; Liu, S.; Xia, L.; Shen, C.; Chu, Y., Normal-inverse bimodule operation Hadamard transform ion mobility spectrometry. *Analytica Chimica Acta* **2018**, *1029*, 44-49.
40. Clowers, B. H.; Belov, M. E.; Prior, D. C.; Danielson, W. F.; Ibrahim, Y.; Smith, R. D., Pseudorandom Sequence Modifications for Ion Mobility Orthogonal Time-of-Flight Mass Spectrometry. *Analytical Chemistry* **2008**, *80* (7), 2464-2473.
41. Tummalacherla, M.; Garimella, S. V. B.; Prost, S. A.; Ibrahim, Y. M., Toward artifact-free data in Hadamard transform-based double multiplexing of ion mobility-Orbitrap mass spectrometry. *Analyst* **2017**, *142* (10), 1735-1745.
42. Hoaglund, C. S.; Valentine, S. J.; Clemmer, D. E., An Ion Trap Interface for ESI-Ion Mobility Experiments. *Analytical Chemistry* **1997**, *69* (20), 4156-4161.
43. Giles, K.; Ujma, J.; Wildgoose, J.; Pringle, S.; Richardson, K.; Langridge, D.; Green, M., A Cyclic Ion Mobility-Mass Spectrometry System. *Analytical Chemistry* **2019**, *91* (13), 8564-8573.
44. Silveira, J. A.; Ridgeway, M. E.; Laukien, F. H.; Mann, M.; Park, M. A., Parallel accumulation for 100% duty cycle trapped ion mobility-mass spectrometry. *International Journal of Mass Spectrometry* **2017**, *413*, 168-175.
45. Garimella, S. V. B.; Ibrahim, Y. M.; Webb, I. K.; Tolmachev, A. V.; Zhang, X.; Prost, S. A.; Anderson, G. A.; Smith, R. D., Simulation of Electric Potentials and Ion Motion in Planar Electrode Structures for Lossless Ion Manipulations (SLIM). *Journal of the American Society for Mass Spectrometry* **2014**, *25* (11), 1890-1896.
46. Hollerbach, A. L.; Li, A.; Prabhakaran, A.; Nagy, G.; Harrilal, C. P.; Conant, C. R.; Norheim, R. V.; Schimelfenig, C. E.; Anderson, G. A.; Garimella, S. V. B.; Smith, R. D.; Ibrahim, Y. M., Ultra-High-Resolution Ion Mobility Separations Over Extended Path Lengths and Mobility Ranges Achieved using a Multilevel Structures for Lossless Ion Manipulations Module. *Analytical Chemistry* **2020**, *92* (11), 7972-7979.
47. Li, A.; Garimella, S. V. B.; Ibrahim, Y. M., A simulation study of the influence of the traveling wave patterns on ion mobility separations in structures for lossless ion manipulations. *Analyst* **2020**, *145* (1), 240-248.

48. Warnke, S.; Ben Faleh, A.; Pellegrinelli, R. P.; Yalovenko, N.; Rizzo, T. R., Combining ultra-high resolution ion mobility spectrometry with cryogenic IR spectroscopy for the study of biomolecular ions. *Faraday Discussions* **2019**, *217* (0), 114-125.
49. Bansal, P.; Yatsyna, V.; AbiKhodr, A. H.; Warnke, S.; Ben Faleh, A.; Yalovenko, N.; Wysocki, V. H.; Rizzo, T. R., Using SLIM-Based IMS-IMS Together with Cryogenic Infrared Spectroscopy for Glycan Analysis. *Analytical Chemistry* **2020**, *92* (13), 9079-9085.
50. Eaton, R. M.; Allen, S. J.; Bush, M. F., Principles of Ion Selection, Alignment, and Focusing in Tandem Ion Mobility Implemented Using Structures for Lossless Ion Manipulations (SLIM). *Journal of the American Society for Mass Spectrometry* **2019**, *30* (6), 1115-1125.
51. Garimella, S. V. B.; Hamid, A. M.; Deng, L.; Ibrahim, Y. M.; Webb, I. K.; Baker, E. S.; Prost, S. A.; Norheim, R. V.; Anderson, G. A.; Smith, R. D., Squeezing of Ion Populations and Peaks in Traveling Wave Ion Mobility Separations and Structures for Lossless Ion Manipulations Using Compression Ratio Ion Mobility Programming. *Analytical Chemistry* **2016**, *88* (23), 11877-11885.
52. Chen, T.-C.; Webb, I. K.; Prost, S. A.; Harrer, M. B.; Norheim, R. V.; Tang, K.; Ibrahim, Y. M.; Smith, R. D., Rectangular Ion Funnel: A New Ion Funnel Interface for Structures for Lossless Ion Manipulations. *Analytical Chemistry* **2015**, *87* (1), 716-722.

”

This method development was critical for execution of IMS/MS selective soft-landing, which will be described in the next section.

2.2 Characterization of Structure and Mass Selected Molecules

Using the high-throughput, high ion utilization efficiency IMS/MS system we performed highly selective material deposition onto a substrate. We characterized the deposited material using several imaging and spectroscopy techniques. We separated isomers of poly-oxo-metallates (POM) using SLIM IMS-MS. Phospho-Tungstic Acid (WPOM) was used as a model molecule. WPOM exists in 5 different Keggin structures as shown in Figure 2.2.1 below.

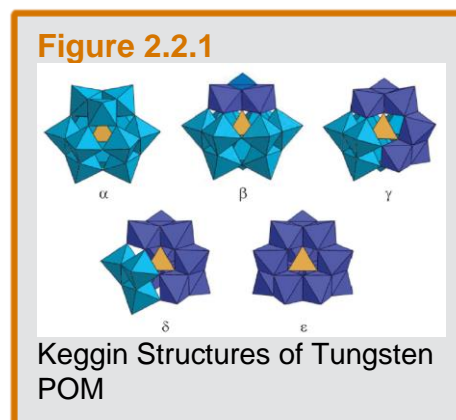
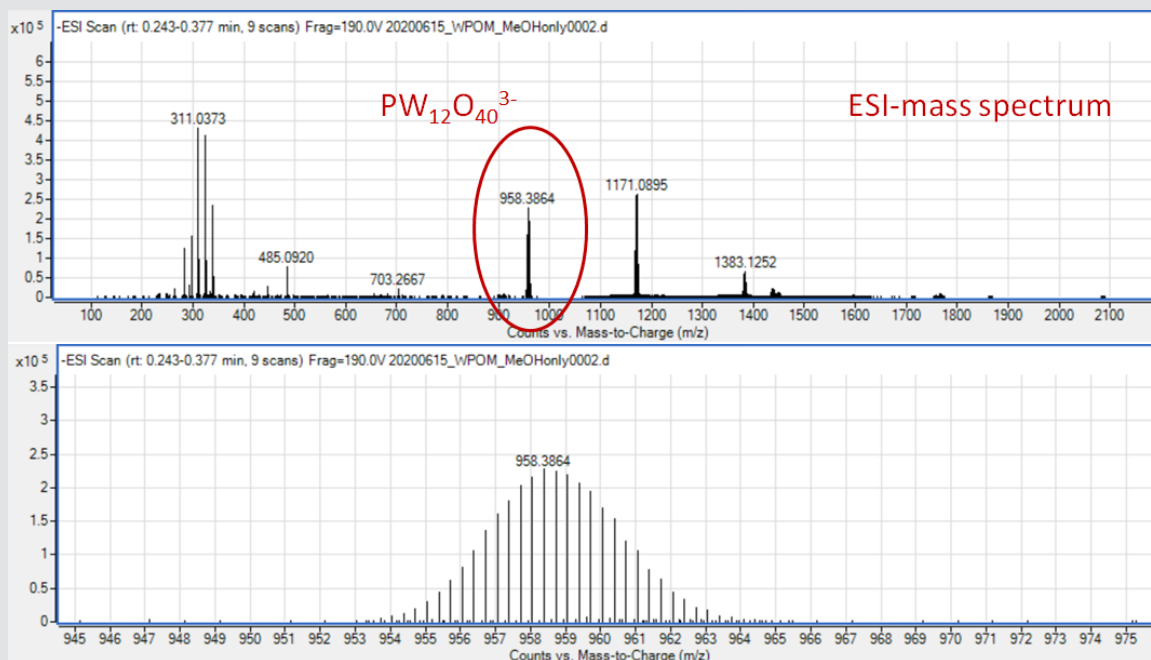


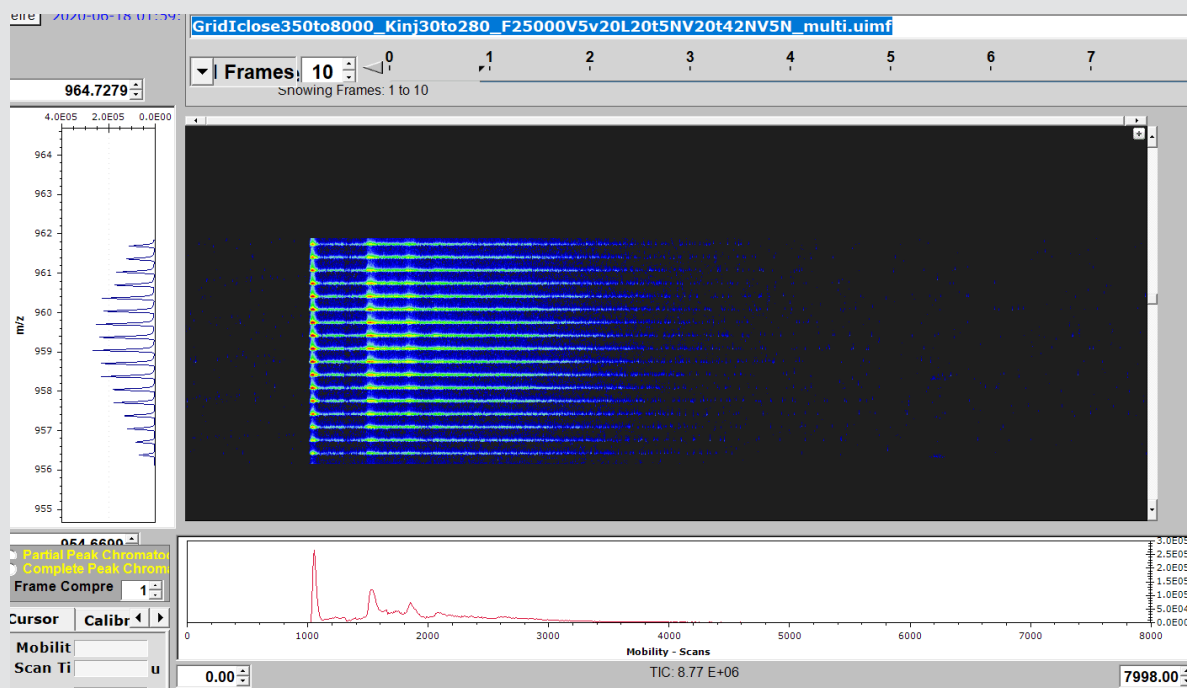
Figure 2.2.2



Mass Spectrum for WPOM. Top panel represents the full mass range. Bottom panel represents the zoomed in spectrum, showing multiplicity of isotope peaks for WPOM.

Using mass spectrometry, we can identify we can identify WPOM using a triply charged peak at m/z 958.4 as shown in the Figure 2.2.1. The above mass spectrum does not show the individual Keggin structures since MS is not sensitive to structural variations of the molecule. However, when the MS system is combined with SLIM system to enable IMS/MS (as described in Section 2.1), we can obtain IMS/MS spectrum. The experimental setup for this IMS/MS experiment is described in detail in Section 2.1 and Figure 1.

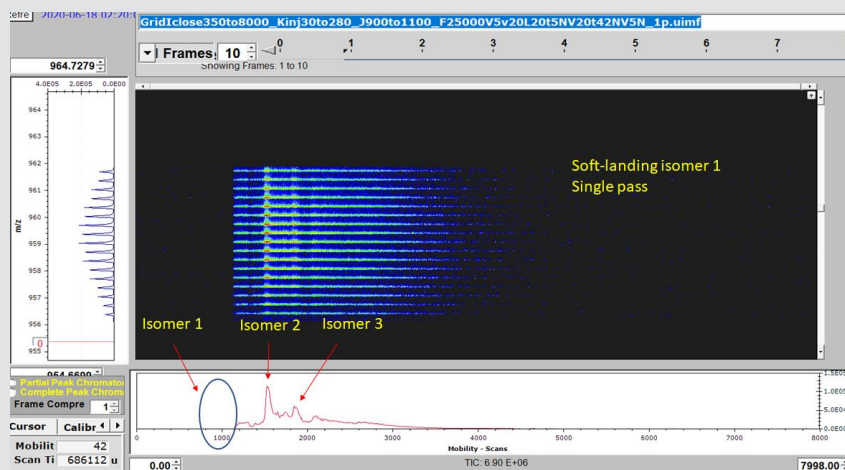
Figure 2.2.3



IMS/MS spectrum for $[\text{PW}_{12}\text{O}_{40}]^{3-}$

Using the SLIM system, the species can now be selected according to their mass and mobility. For example, when the first mobility peak shown in the Figure 2.2.23 above needs to be selected, then it can be switched in the SLIM system to be routed to the deposition plate connected to a current amplifier (see Figure 1) to perform soft-landing. The electric field between SLIM and the deposition plate is 30 V/cm (150 Volts drop over 5 cm) providing a low kinetic energy for the ions (0.03 eV) to deposit them without surface induced structural modification. The deposited current and the IMS spectrum corresponding to the ions after IMS/MS selective switching is shown in Figure 2.2.4.

Figure 2.2.4



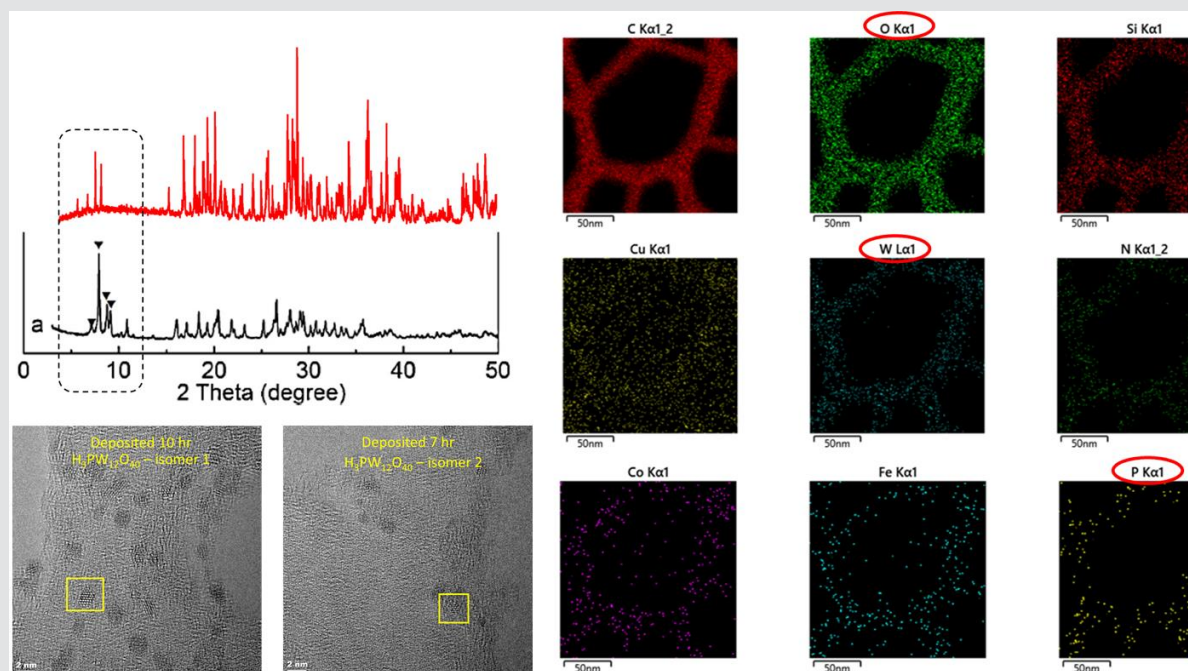
Isomer 1
7.2E6 ions/hr

Isomer 2
3.9E6 ions/hr



IMS/MS spectrum for $[PW_{12}O_{40}]^{3-}$ with isomer 1 switched to deposition. The bottom panel (left) shows the soft-landing current on a substrate for isomer 1. The bottom panel (right) shows soft-landing current for isomer 2. The exact identification of these isomers for their Keggin structures (per Figure 2.2.1) is currently work in progress. The labels represent the number of ions deposited for each species over a 1 hour time span

Figure 2.2.5



Top left panel indicates the XRD spectrum of raw sample of POM in red and it compares to the standard XRD spectrum shown in black.

Bottom left shows the individual isomers (seen in Figure 2.2.4) deposited for 10 hours and 7 hours. The atomic arrangements of the Tungsten atoms are visible.

Right panel shows the EDS spectrum. All the individual atomic constituents of POM are present on the circle corresponding to the copper mesh substrate on which deposition was executed. Other contaminants are distributed even in the central region of the circle representing their prior presence on the substrate; whereas the atoms of POM are present only on the Cu mesh surface. This proves that we are depositing the selected species without ambiguity.

The deposited species were studied using various techniques like XRD, EDS and TEM. IR and CV characterization is ongoing. These data once processed are expected to reveal distinct identification of the deposited isomers and their electrochemical properties. Currently we have a manuscript in preparation to submit this work as a journal article.

3. Ambient Ion Confinement

Since the ability to select and deposit molecules with mass and structural specificity has been demonstrated above, it would greatly benefit being able to demonstrate this under ambient conditions. Typically, the previous experiments described above have been done under vacuum of 3 torr and below. This is owing to the requirement of such vacuum to confine ions using radio-frequency electric fields. At higher pressures than 10 torr, radio-frequencies of voltages are ineffective in confinement of ions. Thus such separations as above are precluded. However, being able to separate ions and collect them at

atmospheric pressure provides distinct advantages of less complicated instrumentation, easier scaling up of the device, more material collection efficiency to name a few.

Here we describe a novel atmospheric pressure ion confinement uses rotating electric fields to move and confine ions inside a segmented ring electrode system at atmospheric pressure. Dynamic electric fields were generated by applying voltages for short periods to subsets of adjacent electrodes and stepping one segment at a time so that the field rotated at a desired rate. Field rotation was accomplished by applying the same phase potentials to adjacent segments on adjacent electrodes (helical rotation). Ion trajectory simulations demonstrate that ions possess secular and micromotions that depend on ion mobility and rotating electric field conditions, respectively. The simulation results were tested experimentally using a 12-cm length APIC device placed in front of a TOF-MS. Ion signals increased when the rotation speed was increased (amplitude was held constant) while ions with different mobilities exhibited maximum intensities at different rotational speeds, consistent with confinement being dependent on field rotation speed. A theoretical model of ion confinement in APIC is discussed.

3.1 Experimental Details

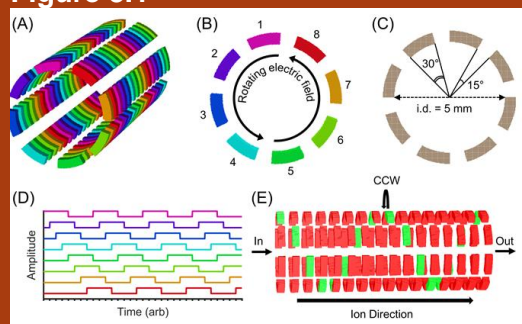
3.1.1 Simulation Parameters

Simulations were performed using SIMION 8.2 (Scientific Instrument Services Inc., Ringoes, NJ, USA) incorporating the statistical diffusion simulation (SDS) collision model. Trajectory qualities were set to a value of 1. To generate an APIC device, conventional stacked ring ion guides were created and each ring was split into 8 individual segments. An isometric view of the segmented ion guide is shown in Figure 1A and a frontal view of the 8 segments comprising a single ring electrode is shown in Figure 1B. Individual segments were colored for clarity. Electrode thicknesses and spacings were 0.5 mm. Device lengths varied between 2.4 cm (24 electrodes) and 16 cm (160 electrodes) and inner diameters were either 3 or 5 mm. The segments of ring electrodes were offset by 45° pitches as drawn from the center of the ion guide (Figure 1C). Seven tetraalkylammonium (TAA) cations were used as model ions (m/z 130, 186, 242, 298, 354, 410, 466). The buffer gas was 760 Torr dry air.

3.1.2 Description of Rotating Waveforms

The rotating waveforms used here were comprised of 8 asymmetric square waves, meaning each wave oscillated between 0 and peak voltage (V_p). Electric fields were rotated about the 8 segments of a ring electrode by shifting the phase of the square wave applied to adjacent segments by 45° . It was possible to use different 'sequences' to describe how many segments were held at V_p at any given moment and how many segments were held at 0 V. For example, a sequence of HHHHLLLL means that at any given time, four segments will possess V_p (e.g. H) and four segments will possess 0 V (e.g. L). An example of eight 45° phase-shifted square waves using a HHHHLLLL sequence is shown in Figure 1D. The segment sequence was also phase-shifted by 45° between adjacent ring electrodes to drive ions through the device. In other words, electric field rotations occur between electrodes as well as between segments of a single electrode. At any given moment, a square wave possessing a single phase forms a helical (or corkscrew) pattern along the axis of the APIC, shown in Figure 1E. A HLLLLLLL sequence is demonstrated for clarity (green electrodes = V_p , red electrodes = 0 Vpp). In all studies presented here, the electric field was rotated in a counterclockwise (CCW) fashion along the axis of ion movement to produce a rotating electric field that also moved forward. Clockwise rotation moved ions in the reverse direction. A video of the potential energy surface produced by a helically rotating electric field over the APIC is given in the Supporting Information (Supporting Video 2).

Figure 3.1



(A) Illustration of the helical APIC design. (B) Frontal view of the 8 segments comprising an APIC electrode and the direction of electric field rotation. (C) Dimensions of a segmented electrode. (D) Diagram showing the eight 45° phase-shifted waveforms applied to each segment. (E) APIC schematic colored to show the orientation of segments on adjacent electrodes using a 1 up 7 down sequence for illustrative purposes. Segments in green possess electric fields with the same phase.

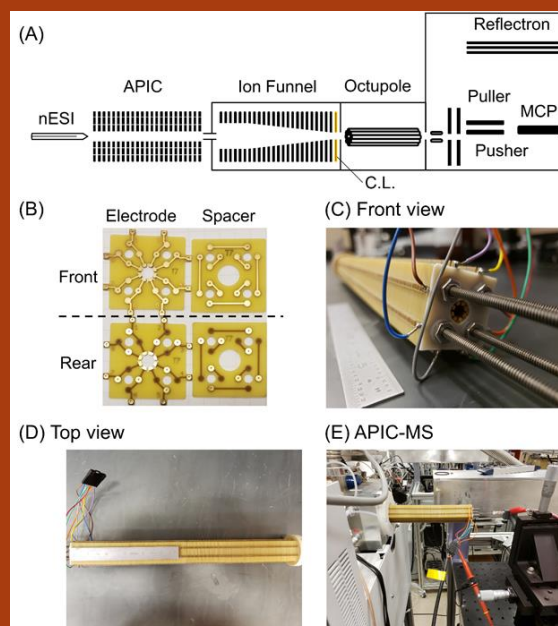


Figure S1: (A) Experimental setup of APIC coupled to a MS. (B) Front and rear views of an APIC electrode and spacer. (C) Front and (D) top views of a fully assembled APIC. (E) APIC mounted to the front of a MS.

emitters (1 – 2 μm o.d.) were pulled from nonfilamented borosilicate glass capillaries (0.85

3.1.3 Electrospray and Mass Spectrometry

The seven tetraalkylammonium halides (TAA_C2-C8) and acetonitrile used in this study were purchased from Millipore-Sigma (St. Louis, MO, USA). A schematic of the experimental setup is given in the Supporting Information (Figure S1A). Nanoelectrospray

mm i.d.; 1.5 mm o.d.) using a P-2000 CO₂ laser-based micropipette tip puller (Sutter Instruments, Novato, CA, USA). All emitters were examined using a light microscope to obtain approximate o.d.'s and to verify tip integrity. Analyte solutions were loaded into the emitters using 10 μ L gel loading tips (BioRad, Hercules, CA, USA). Electrical contact was made to solutions via a silver wire embedded into a microelectrode holder (model ESW-M15N, Warner Instruments, Hamden, CT, USA). Emitters were mounted to a 3D printed custom holder which was placed on top of a 3-axis stage (Thorlabs Inc, Newton, NJ, USA). Emitters were placed approximately 5-10 mm away from the APIC entrance. Ions generated by nanoESI were captured using a custom flared inlet capillary. An ion funnel (RF = 200 V_{pp}, 1 MHz; P = ~1 Torr air) and conductance limiting orifice (2.5 mm i.d.) was placed between the capillary and the octupole of a 6224 Agilent TOF-MS.

3.1.4 APIC Fabrication

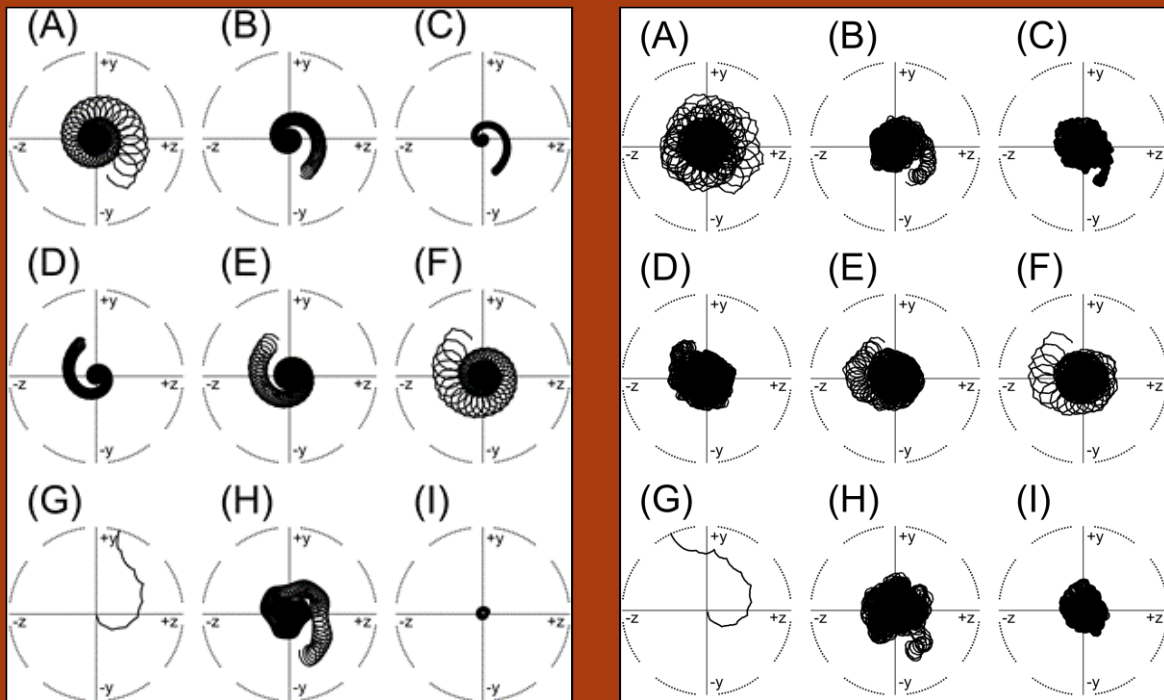
APIC electrodes with i.d. 5 mm were constructed using PCB technology. Photographs of the individual APIC electrodes, spacers, and fully assembled APIC are provided in the Supporting Information (Figure S1B, Figure S1C, Figure S1D). Four holes were cut into each electrode and spacer to allow for device assembly and mounting to a mass spectrometer. The spacers were used to couple the waveforms applied to the segments of the electrode in front of the spacer to the next segments of the electrode behind the spacer. For example, a spacer takes the waveform applied to segment 1 of electrode 1 and routes it to segment 2 of electrode 2. The next spacer takes the same waveform applied to segment 2 of electrode 2 and routes it to segment 3 of electrode 3, etc. Experiments were performed in the open air without an enclosure. Figure S1E shows a photograph of the APIC assembly in front of the mass spectrometer.

3.2 Results and Discussion

3.2.1 Ion Trajectory Simulations

Figure 2A shows the trajectory of a single TAA_C6 ion (m/z 354.5; $K_0^{(N_2)} = 1.02$ cm²/(V*s),) traversing a 16-cm long helical APIC using electric field conditions of 400 V_{pp}, 30 kHz, and a HHHHLLLL sequence. The simulation was performed with the ion initially positioned off-center (i.e. in the bottom right quadrant). Simulated diffusion was omitted in this study to better observe ion motion. According to the simulation, ions exhibit two types of motion in helically rotating electric fields: (1) a spiral-like secular ion motion, and (2) smaller micromotions (also spiral-like) that rotate about the secular motion. As ions traverse the APIC, they spiral inwards until they reach an equilibrium point at the center of the device. The radius of this equilibrium point appears to be the same as the micromotion radius. It was possible to change the micromotion radius by varying the electric field rotational frequency. For example, increasing the frequency to 50 kHz while

Figure 3.2



(Left)

Ion trajectories of a single TAA_C6 ion (m/z 354.5) using (A) 30, (B) 50, and (C) 100 kHz at 400 V_{pp} , (D) 400, (E) 600, and (F) 800 V_{pp} at 60 kHz, (G) 700 V_{pp} and 30 kHz, (H) 400 V_{pp} sine wave at 30 kHz, and (I) 600 V_{pp} at 100 kHz without considering diffusion. Sequence = HHHLLLLL, i.d. = 5mm, pressure = 760 Torr dry air, length = 16 cm.

(Right)

Ion trajectories of a single TAA_C6 ion (m/z 354.5) using (A) 30, (B) 50, and (C) 100 kHz at 400 V_{pp} , (D) 400, (E) 600, and (F) 800 V_{pp} at 60 kHz, (G) 700 V_{pp} and 30 kHz, (H) 400 V_{pp} sine wave at 30 kHz, and (I) 600 V_{pp} at 100 kHz without considering diffusion. Sequence = HHHLLLLL, i.d. = 5mm, pressure = 760 Torr dry air, length = 16 cm.

keeping amplitude and sequence the same resulted in a smaller micromotion radius, shown in Figure 2B. Again, the ion begins in the bottom right quadrant and spirals inward towards the center of the APIC where it is confined at the center with a radius similar to the micromotion radius. Further increasing the frequency to 100 kHz resulted in an even smaller micromotion radius, shown in Figure 2C. Using frequencies lower than about 30 kHz resulted in ion loss to the electrodes when all other parameters were held constant. This suggests that ions must orbit below a certain boundary radius to maintain stability inside the APIC (discussed later). In contrast, ion trajectories generated using higher frequencies (e.g. 200 kHz at 400 Vpp) did not possess any easily discernable secular motion or micromotions. Presumably ions must possess both types of motion to efficiently traverse the helical APIC, or it is likely they will be lost in practice. The amplitude of the rotating electric field similarly affects micromotion radius. As shown in Figure 2D, the use of 60 kHz, HHHLLLLL sequence, and 400 Vpp results in small micromotions. The

micromotion radius increases when amplitude is increased to 600 Vpp (Figure 2E) and further increases when 800 Vpp is applied (Figure 2F).

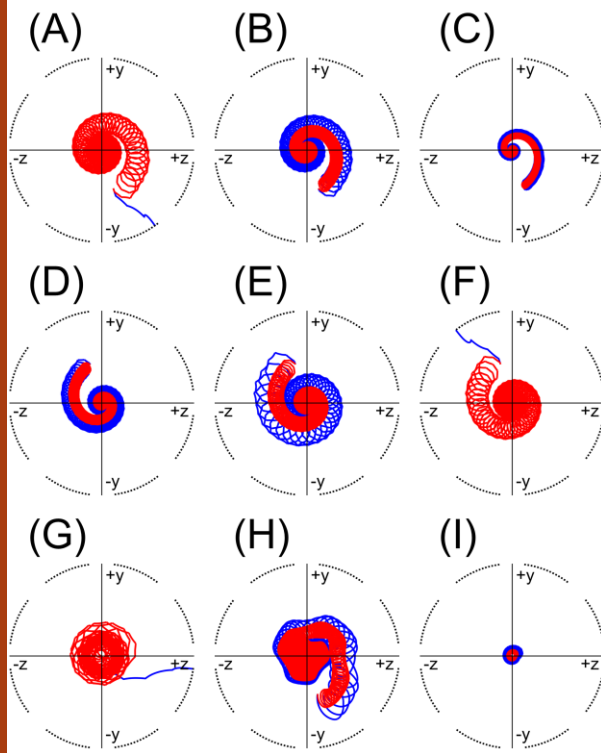
The large micromotion radii associated with lower frequencies and higher amplitudes suggests that ions maintain stability over a defined range of conditions and become unstable inside the APIC if those conditions are exceeded. The ion trajectory in Figure 2G shows an ion being lost to the electrodes when frequency and amplitude were set to 30 kHz and 600 Vpp, respectively. Note the ion was initially positioned at the center of the APIC to ensure that an off-center starting position did not contribute to ion loss. As can be seen, the micromotion radius under these conditions is larger than the stable boundary radius, and this forces the ion into an unstable trajectory that will result in its ejection from the APIC. We also note that space charge will contribute to the tendency of an ion to approach the boundary radius, but space charge was not considered in these simulations.

In addition to frequency and amplitude, waveform type (e.g. square, sine, etc.) also affects ion motion inside APIC. Figure 2H shows the ion trajectory obtained using sine waves of 30 kHz and 400 Vpp. Compared to square waves possessing the same frequency and amplitude, the micromotion radii are noticeably smaller, but are larger than the micromotion radii obtained using 50 kHz square waves. Also noteworthy is that the ion does not exhibit a purely helical secular motion but rather some combination of shapes, resembling something like a spiral following the corners of a triangle. This suggests that square waves influence ion motion more strongly than sine waves and harsher sine wave conditions (i.e. lower frequency / higher amplitude) must be used to obtain the same trajectories as square waves. The micromotions obtained using sine waves also appear smoother than they do using square waves, although the significance of this is unclear. For conciseness, all other experiments in this study utilized a HHHLLLL square wave sequence, though in-depth studies of other waveform types will be reported in the future. The final panel in Figure 2 (Figure 2I) shows a trajectory of an ion starting at the center of the APIC using waveform conditions of 100 kHz, 600 Vpp, and HHHLLLL square waves. The ion is strongly confined to the center of APIC, illustrating that ions are better confined at higher frequencies because their micromotion radius is smaller, but higher amplitudes are needed to maintain ion secular motions and micromotions.

For comparison, simulations utilizing diffusion and the same conditions as in Figure 2 are shown in the Supporting Information (Figure S2). All nine trajectories show the same relative secular motion and micromotion trends as those observed without diffusion. The main difference between the two figures is that ion motions are somewhat obscured by the randomness created by the diffusion parameter. The main point is that ions are confined in APIC even when diffusion is included.

Trajectory simulations showcasing ion mobility effects were performed using the tetraalkylammonium cations TAA_C4 (m/z 242.1, $K_0(N_2)=1.33 \text{ cm}^2/(V*s)$) and TAA_C8 (m/z 466.5, $K_0(N_2)=0.84 \text{ cm}^2/(V*s)$), and overlaid plots are shown in the Supporting Information (Figure 3). Diffusion was omitted again for ease of visualization. The trajectory of the TAA_C8 ion (red trace, Figure 3) resembles the trajectory of the TAA_C6 ion previously shown in Figure 2A in that the ion spirals inwards towards the APIC center with micromotions rotating about the secular motion (Figure 3A). In contrast, the smaller TAA_C4 ion (blue trace) is immediately ejected from the APIC under the same electric conditions and starting position. However, as shown in Figure 3B and Figure 3C,

Figure 3.3

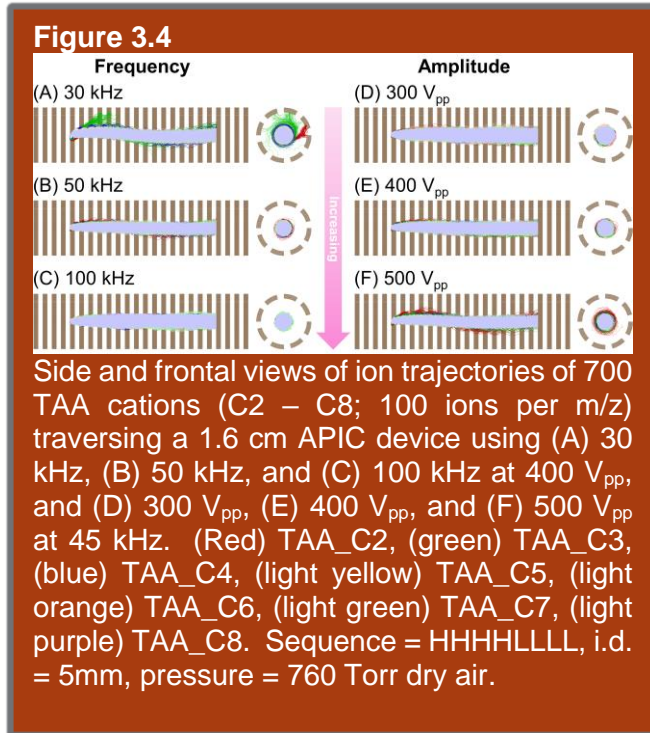


Ion trajectories of a single TAA_C4 (blue traces, m/z 242.1) and TAA_C8 ions (red traces, m/z 466.5) using (A) 30, (B) 50, and (C) 100 kHz at 400 V_{pp} , (D) 400, (E) 600, and (F) 800 V_{pp} at 60 kHz, (G) 700 V_{pp} and 30 kHz, (H) 400 V_{pp} sine wave at 30 kHz, and (I) 600 V_{pp} at 100 kHz without considering diffusion. $L = 16$ cm, $P = 760$ Torr dry air.

it is possible to generate confinement conditions for the TAA_C4 ion by using higher frequencies. Similarly, applying high amplitudes results in the loss of TAA_C4 and the retention of TAA_C8 while the use of lower amplitudes provides confinement of both ions (Figure 3D, Figure 3E, Figure 3F). A notable feature of Figure 3 is that ions with different mobilities possess micromotions with different radii under the same conditions. The radii of both ions change with frequency and amplitude, but the micromotion radius of the higher mobility ion is always larger than the micromotion radius of the lower mobility ion. Clearly high mobility ions are more easily perturbed by the rotating electric field compared to low mobility ions. Additionally, lower mobility species rotate more frequently (i.e. number of micromotions) per unit distance than higher mobility ions. This indicates that rotating electric fields provide better confinement for ions that exhibit more micromotions per unit distance (e.g. low mobility ions).

Simulations of a TAA mixture (C2 - C8, 100 ions per m/z) were also performed to obtain a general picture of the ion

trajectories. Side and frontal views of overlaid TAA ion trajectories using 30, 50, and 100 kHz (450 V_{pp} , HHHHLLLL) and 300, 400, and 500 V_{pp} (45 kHz, HHHHLLLL) are shown in Figure 4. All simulations incorporated ion diffusion. Ions were birthed 4 mm inside the APIC and were allowed to traverse 1.6 cm. The side view obtained using 30 kHz frequency and 450 V_{pp} (Figure 4A) shows significant ion losses associated with TAA_C2 (red) and TAA_C3 (green), in line with previous simulations. The frontal view shows that TAA_C2 ions are lost almost immediately upon starting the simulation, thus indicating no significant ion confinement. In contrast, two-thirds of the TAA_C3 ions are lost shortly after beginning the simulation. A few of the surviving TAA_C3 ions exhibit exceptionally large oscillations that correspond to unstable trajectories, ultimately resulting in their loss. Less than one-third of the starting TAA_C3 ions survive the simulation. The larger TAA ions traversed the helical APIC without loss (i.e. TAA_C4 (blue), TAA_C5 (light yellow), TAA_C6 (salmon), TAA_C7 (light green), TAA_C8 (light purple)). Note that the ion spot diameter at the APIC center is smaller for lower mobility ions. As frequency is increased to 50 kHz while maintaining amplitude and sequence (Figure 4B), all TAA ions remain



confined inside the APIC, though the TAA_C2 ions possess a noticeably larger orbit about the center of the APIC. Further increasing frequency to 100 kHz results in ion trajectories almost completely overlapping (Figure 4C).

Similar trends based on ion mobility are observed when varying amplitude (at 45 kHz, HHHHLLLL). Simulations performed using 300, 400, and 500 V_{pp} amplitudes (Figure 4D, Figure 4E, Figure 4F) showed confinement for all TAA ions except for one TAA_C2 ion at 500 V_{pp}, which appears to be in the process of being ejected. This suggests that the TAA_C2 ion is on the edge of the stability region inside the APIC. Furthermore, these simulations show that a reasonably wide range of ions with different mobilities (e.g. TAA_C2 – TAA_C8) can be confined using rotating electric fields.

3.2.2 Theory of ion motion inside APIC

The theoretical description of voltages and stable ion trajectories inside APIC has been developed based on non-linear stability analysis theory, for the case where half of the electrodes are supplied with a high voltage and the other half are grounded, as shown in Figure 3.1. A snapshot of this is shown in Figure below. A full description of the theoretical methods will be the subject of the manuscript in preparation, where it will be disclosed comprehensively. The terms carry their usual notation in this context (e.g. U is voltage inside APIC, U₀ is the applied voltage on the APIC electrode, R is normalized radius, K_{reduced} is ion's reduced mobility, w is the angular velocity of the rotating wave, r₀ is the radius of the APIC device).

$$U(R, \theta) := U_0 \cdot \left[1 + \sum_{n=1}^{\infty} \left[\frac{2}{\pi} \left(\frac{1}{n} R^n \sin(n \cdot \theta) \right) \right] \right] \quad \text{Voltage inside APIC in cylindrical co-ordinates}$$

The velocity of ions inside APIC due to the voltage supplied above

$$E_r(R, \theta) := K_{\text{reduced}} \cdot U_0 \cdot \left[\sum_{n=1}^{\infty} \left(\frac{2}{\pi \cdot r_0} R^{n-1} \sin(n \cdot \theta) \right) \right]$$

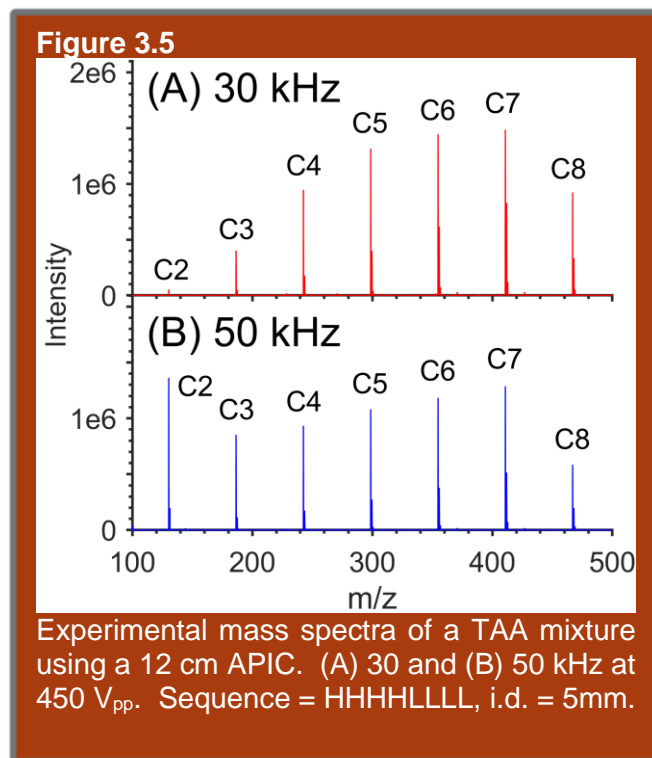
$$E_t(R, \theta) := K_{\text{reduced}} \cdot U_0 \cdot \left[\sum_{n=1}^{\infty} \left(\frac{2}{\pi \cdot r_0} R^{n-1} \cos(n \cdot \theta) \right) \right] - r_0 \cdot R \cdot \omega$$

Nonlinear stability analysis yield conditions for stable ion trajectories such that a minimum angular velocity is essential to maintain ion trajectory stably trapped inside APIC volume. The expression for the same is

$$\omega > \frac{8 \cdot K_{\text{reduced}} \cdot U_0}{\pi \cdot r_0^2}$$

The co-relations from the theory, i.e. the minimum angular velocity of wave needed, the mobility range of ions that are effectively confined and the effect of increasing the radius co-relate well between theory and experiment and simulations. The experimental results are detailed in the subsequent sections.

3.2.3 Experiments using helically rotating electric fields

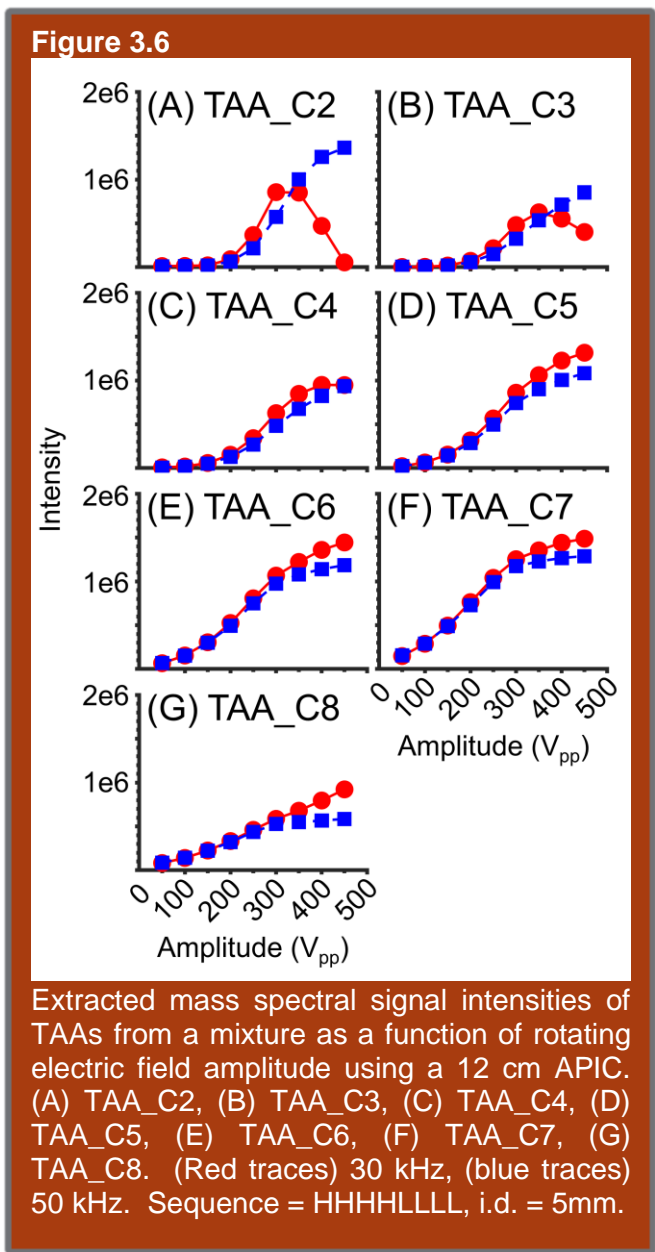


To test the simulation results, a 12 cm stacked ring ion guide with segmented ring electrodes was constructed and placed in front of a TOF-MS. A mixture of seven TAAs (C2 – C8, 100 μM each TAA) in acetonitrile were introduced via nanoelectrospray ionization. Figure 5a and Figure 5B show mass spectra acquired using frequencies of 30 and 50 kHz (at 450 V_{pp}, HHHLLLLL), respectively. As can be seen, all seven TAAs were observed in both experiments. It is noteworthy that the peaks corresponding to TAA_C2 and TAA_C3 were significantly lower in intensity than the other TAA cations when 30 kHz was used, even though all TAAs were present

in solution at equimolar concentrations. However, increasing the frequency to 50 kHz resulted in much greater signal intensities for the smaller ions and even established TAA_C2 as the base peak. The signal intensities of the TAA_C4 - TAA_C7 ions did not change significantly with the associated change in frequency, although a small decrease in signal intensity was observed for the TAA_C8 ions. These observations are in line with simulations which also showed that higher frequencies were needed to confine higher mobility ions and lower frequencies for lower mobility ions. We note that the helical APIC possessed a 5 mm i.d. and therefore cannot rule out space charge contributions to ion losses. We aim to address space charge in future embodiments. We also note that the combination of 450 Vpp and 100 kHz could not be used for extended time periods due to power supply limitations.

Experiments were also performed where the amplitude of the rotating electric field was varied from 50 to 450 Vpp in 50 Vpp increments using 30 and 50 kHz frequencies (HHHHLLLL sequence). The maximum MS intensities for each TAA at each amplitude and frequency combination were extracted and plotted in Figure 6. Data acquired using 30 kHz are shown in red and 50 kHz in blue. The

maximum signal intensity obtained for TAA_C2 (Figure 6A) using 30 kHz was at 300 Vpp while the maximum for 50 kHz was at 450 Vpp. While the TAA_C2 signal intensity continually increased with increasing amplitude using 50 kHz, significant signal loss occurred when 30 kHz and 400 Vpp was used, and the signal was almost depleted upon further increasing amplitude to 450 Vpp. Similar trends in signal intensity were observed for TAA_C3 (Figure 6B), though losses were not as drastic compared to TAA_C2. It is worth noting that the largest signal intensities for TAA_C2 and TAA_C3 were obtained when higher frequencies were used (i.e. 50 kHz > 30 kHz), once again in line with simulations. In contrast, both frequencies provided approximately equal signal intensities for TAA_C4 over the range of amplitudes studied (Figure 6C). As m/z increased, opposite trends in the signal intensities obtained using 30 and 50 kHz were observed. For



example, the TAA_C5 signal obtained using 30 kHz and 450 Vpp was about 22% higher than obtained using 50 kHz and the same amplitude (Figure 6D). TAA_C6, TAA_C7, and TAA_C8 also showed higher signal intensities when 30 kHz was used (Figure 6E, Figure 6F, Figure 6G). It is likely that higher frequencies and amplitudes (above 450 Vpp) would provide better signal intensities over the range of TAAs studied, up to the charge capacity of the APIC.

4. Publications, Patents and Proposals

1. Ion mobility spectrometry with high ion utilization efficiency using traveling wave based structures for lossless ion manipulations (ALIM), Li et al, in review
2. Methods of ion focusing using non-linear DC fields, non-provisional patent application submitted to USPTO
3. Methods for mass and structure selective material synthesis, provisional patent submitted to USPTO. (non-provisional patent due to be submitted next year)
4. Ion Confinement under ambient conditions, Hollerbach et al, in preparation
5. Mass and structure selective molecular ion soft-landing, Li et al, in preparation
6. NIH R01 grant application, to be submitted under Biomaterials study group, scope of work to include soft-lading of biomolecules to study molecular assemblies and their implications for novel biomaterials, in preparation

Pacific Northwest National Laboratory

902 Battelle Boulevard
P.O. Box 999
Richland, WA 99354
1-888-375-PNNL (7665)

www.pnnl.gov